TAMPERE UNIVERSITY OF TECHNOLOGY

ANNINA SAUKKO

A Dual Contrast Method for Computed Tomography Imaging of Cartilage Injuries

Master of Science Thesis

Examiner: Professor Ilpo Vattulainen
Tarkastaja ja aihe hyväksytty
Luonnontieteiden tiedekuntaneuvoston
kokouksessa 4.11.2015

TIIVISTELMÄ

TAMPEREEN TEKNILLINEN YLIOPISTO
Teknis-luonnontieteellinen koulutusohjelma
SAUKKO, ANNINA: Nivelrustovammojen kuvantaminen kaksoiskontrastiainetehosteisella tietokonetomografia-menetelmällä
Diplomityö, 63 sivua
Toukokuu 2016
Pääaine: Teknillinen fysiikka
Tarkastaja: Professori Ilpo Vattulainen
Ohjaajat: FM Juuso Hokanen, FT Mikael Turunen
Avainsanat: nivelrusto, rustovamma, post-traumaattinen nivelrikko, kontrastitehosteinen tietokonetomografia, kuvantaminen, varjoaine, diffuusio

Nivelruston vammojen varhainen diagnosointi on tärkeää, sillä vammojen kirurginen hoito aikaisessa vaiheessa voi ehkäistä post-traumaattisen nivelrikon syntymisen. Nykyiset diagnostiset keinot, jotka perustuvat magneettikuvaukseen, niveltähystykseen, perinteiseen röntgenkuvaukseen sekä kliiniseen tutkimukseen, eivät kuitenkaan ole tarpeeksi herkkiä havaitsemaan ruston tuoretta vammaa tai sen laukaisemaa ympäröivän kudoksen alkavaa rappeumaa.

Kontrastitehosteinen tietokonetomografian on osoitettu soveltuvan nivelruston vammojen varhaiseen diagnosointiin. Menetelmä vaatii kuitenkin kaksi kuvausta ruston kunnon määrittämiseen: ensimmäinen kuvaus heti ja toinen 45 minuuttia sen jälkeen kun varjoaine on annosteltu nivelrakoon. Ensimmäinen kuvaus tarvitaan nivelruston segmentointiin ja ruston vaurioiden diagnosointiin, kun taas jälkimmäinen kuvaus mahdollistaa vammaa ympäröivän kudoksen mahdollisen post-traumaattisen rappeuman arvioinnin. Nivelruston segmentointi 45 minuutin kuvista on haastavaa, sillä kontrasti nivelnesteen ja ruston rajapinnassa pienenee huomattavasti varjoaineen diffuusion vuoksi.

Kahden ajastetun kuvauksen suorittaminen on logistisesti hankalaa ja lisää potilaan säteilyannosta. Tätä varten olemme kehittämässä uutta kaksoiskontrastiainetta, jonka avulla ruston ja nivelnesteen rajapinnan kontrasti pysyy myös 45 minuutin kuvissa erittäin hyvänä. Tämä mahdollistaa rustovaurioiden segmentoinnin sekä ympäröivän ruston laadun arvioinnin yhtäaikaisesti 45 minuutin kuluttua kaksoiskontrastiaineen annostelusta. Kehitettävä menetelmä voi parantaa rustovaurioiden diagnostiikkaa ja siten antaa mahdollisuuden vammojen varhaiseen kirurgiseen korjaukseen post-traumaattisen nivelrikon ehkäisemiseksi. Lisäksi menetelmä puolittaa potilaaseen kohdistuvan säteilyannoksen.

ABSTRACT

TAMPERE UNIVERSITY OF TECHNOLOGY
Degree Programme in Science and Engineering
SAUKKO, ANNINA : A Dual Contrast Method for Computed Tomography Diagnostics of Cartilage Injuries
Master of Science Thesis, 63 pages
May 2016
Major: Technical Physics
Examiner: Professor Ilpo Vattulainen
Supervisors: M.Sc. Juuso Honkanen, Ph.D. Mikael Turunen
Keywords: Articular cartilage, cartilage injury, post-traumatic osteoarthritis, contrast enhanced computed tomography, imaging, contrast agent, diffusion

The diagnostics of fresh cartilage injuries in the early-state is important for the prevention of post-traumatic osteoarthritis (PTOA). Currently, the sensitivity of diagnostic techniques, including magnetic resonance imaging (MRI), clinical examination, native X-ray imaging, and arthroscopic examination, have not been sufficient for detecting fresh cartilage injuries or the incipient degeneration of the tissue surrounding the injury.

Contrast enhanced computed tomography (CECT) enables the detection of fresh cartilage injuries. However, it requires two images first one immediately after the contrast agent administration into synovial fluid and second one 45 minutes after the administration. The first image allows the accurate segmentation of the cartilage surface since contrast agent diffusion diminishes the contrast at the cartilage-synovial fluid interface soon after contrast agent administration. Delayed imaging, at 45 minutes after the administration, enables the detection of cartilage injuries and degenerations as elevated contrast agent concentration at injured or degenerated tissue.

Performing two scheduled imaging is logistically challenging and it doubles the patient exposure to the radiation. Therefore, in this thesis we develop a dual contrast method that will allow the diagnostics of fresh cartilage injuries and degeneration of the surrounding tissue conducting only one image 45 minutes after dual contrast agent administration. As a result, this method will enhance the CECT diagnostics of fresh cartilage injuries among with other joint diseases, thus leading to better repair and prevention of PTOA. Furthermore, the radiation dose will be significantly reduced as compared to the current method used in CECT diagnostics of a knee joint and the imaging will be relieved logistically.

PREFACE

On June 2015 I started this project as part of my research work on contrast enhanced computed tomography in the Biophysics of Bone and Cartilage Group at the University of Eastern Finland but it turned out to be a long battle against the nano world. This thesis is the outcome of this long process; the long days spent in the lab and numerous attempts hoping for good results. Even though it was a long and rocky road here, this project has encouraged me to continue researching in medical physics as a post-graduate student.

First of all, I would like to express my deepest gratitude to Prof. Juha Töyräs for his endless support and help during this project and for giving me the opportunity to work with such a interesting research subject. I would also like to thank my supervisors M.Sc. Juuso Honkanen and Ph.D. Mikael Turunen for their patient guidance, advice, and encouragement. I also wish to thank Ph.D. Wujun Xu and Prof. Vesa-Pekka Lehto, without whose cooperation I would have been unable to develop the nanoparticle suspension. I would like to thank the head of the BBC Group Prof. Jukka Jurvelin and all the members of BBC Group. I have been extremely lucky to have the opportunity to work in such an innovative environment with such amazing people around.

I would like to thank my mother, father, and brother for all the love and support during my studies. Completing this thesis would not be possible without you. Finally, Sami deserves a particular note of thanks for his continued support and encouragement in ups and downs of my research.

Tampere, May 2016

Annina Saukko

CONTENTS

SYMBOLS & ABBREVIATIONS

A	Atomic mass
AMPR	Adaptive Multiple Plane Reconstruction
AuNP	Gold nanoparticle
Bi_2O_3	Bismuth oxide
BiNP	Bismuth nanoparticle
C	Concentration
C_i	CT number in voxel i
CBCT	Cone-beam computed tomography
CECT	Contrast enhanced computed tomography
Cl^-	Cloride ion
CT	Computed tomography
D	Diffusion coefficient
d	Diameter
d_{od}	Object-detector distance
d_{os}	Object-source distance
E	X-ray energy
ECM	Extracellular matrix
EDTA	Ethylenediaminetetraacetic acid
F	Faraday constant
FCD	Fixed charge density
GAG	Glycosaminoglygan
HU	Hounsfield unit
I	Intensity
J	Diffusion flux

K^+	Potassium ion
KCl	Potassium chloride
KH_2PH_4	Monopotassium phosphate
kVp	Peak kilovoltage
L	Object size
$L^{'}$	Magnified object size
M	Magnification
microCT	X-ray microtomography
MRI	Magnetic resonance imaging
N	Total amount of photons
Na^+	Sodium ion
NaCl	Sodium cloride
Na_2HPO_4	Sodium hydrogen phosphate
OA	Osteoarthritis
PBS	Phosphate-buffered saline
PET	Positron emission tomography
PG	Proteoglycan
PdI	Polydispersity index
PEG	Polyethylene glycol
pQCT	Peripheral quantitative CT
PTOA	Post-traumatic osteoarthritis
q	Electric charge
R	Gas constant
R^-	Generic ion
r	Donnan ratio

ROI	Region of Interest
SPECT	Single-photon emission tomography
T	Temperature
t	Time
x	Distance travelled in the medium
w. w.	Wet weight
Z	Atomic number
z	Valence of a ion
μ	Linear attenuation coefficient
ρ	Density
Ψ	Membrane potential

1. INTRODUCTION

Articular cartilage covers the ends of articulating bones, such as femur and tibia. Its damage is a relatively common injury and can cause joint pain, swelling, and immobility. The damage can also initiate post-traumatic osteoarthritis (PTOA) [1, 2]. PTOA is a joint disease in which articular cartilage degenerates gradually. Recent findings suggest that pharmaceutical interventions, in addition to surgical interventions, can be used to prevent the development of PTOA but only if the injury is detected early [3–5]. Thus, for effective surgical or pharmaceutical treatment and prevention of PTOA, early diagnostics of cartilage injury is important. With current diagnostic techniques, including magnetic resonance imaging (MRI), clinical examination, native X-ray imaging, and arthroscopic examination, the detection of fresh cartilage injuries and changes in surrounding tissues is difficult or even impossible. Moreover, the current techniques can only detect late-state and advanced tissue changes. For this reason, new enhanced diagnostic methods for detection and grading of cartilage injuries would improve the early selection of treatment, thus reducing the risk for PTOA.

In contrast enhanced computed tomography (CECT) imaging, contrast agents are introduced to enhance the interface of the synovial fluid and cartilage, as the natural contrast in X-ray at this interface is almost non-existent. Superficial collagen disruption, proteoglycan (PG) loss, and increased water content are the first signs of cartilage injury [6, 7]. They increase the permeability of the tissue, thereby affecting diffusion of contrast agents into articular cartilage [8, 9]. By observing changes in contrast agent diffusion into cartilage, acute injuries can be detected using CECT [10, 11]. CECT imaging of a knee joint can be conducted using cone beam CT (CBCT) scanner. It utilizes a conical X-ray beam to acquire images covering a large volume with a single rotation around the knee. The main advantages of CBCT are low radiation doses and a high resolution [12].

In a recent study, CECT was applied *in vivo* for the first time [10]. The study concluded that the maximum contrast agent concentration in the cartilage was achieved at 30–60 min after the injection into the joint. Currently, CECT of a knee joint is conducted immediately after and at 45 minutes after contrast agent injection into the synovial fluid. The first image is needed for accurate segmentation of the cartilage surface since contrast agent diffusion diminishes the contrast at the cartilage-synovial

fluid interface. Delayed imaging, at 45 minutes after the administration, is required for the detection of cartilage injuries due to elevated contrast agent concentration at injured or degenerated tissue.

The X-ray computed tomography (CT) diagnostics of articular cartilage injuries can be improved significantly by introducing a novel dual contrast method. In this thesis, a dual contrast agent containing a mixture of an iodine-based contrast agent (ioxaglate) and suspension of nano-sized bismuth oxide particles is developed and employed for evaluation of cartilage injuries. We hypothesize that since these nanoparticles are relatively large (90-210 nm in diameter), they are unable to diffuse into cartilage; therefore, the contrast at the interface between synovial fluid and cartilage can be retained at high level due to the nanoparticles, even at the 45 minutes after the contrast agent administration. Ioxaglate, on the other hand, is required since its diffusion into cartilage allows the quantitative evaluation of the tissue composition. Bismuth oxide nanoparticles (BiNPs) are selected for this study due to their high X-ray attenuation coefficient, inexpensive price, and low toxicity [13].

The aim of this study is to verify the potential of the dual contrast method by imaging intact and injured osteochondral plugs using a X-ray microtomography (microCT). We hypothesize that the dual contrast method will provide diagnostic information non-reachable with any current diagnostic modality. In clinical use, this technique may lead to better diagnostics of various joint conditions, especially with fresh cartilage injuries, thus leading to better repair and prevention of PTOA. As a result, the radiation dose will be significantly reduced as compared to the current method used in CECT diagnostics of a knee joint. In addition, the application of the dual contrast method will potentially improve image quality allowing the fully automatic segmentation of the CBCT knee joint images. This would enhance the diagnostics of various joint conditions, but also enable more straightforward modelling of the joint function and the planning of interventions.

2. ARTICULAR CARTILAGE

Articular cartilage is a highly specialized connective tissue covering the ends of articulating bones, such as femur and tibia [14, 15]. It provides a smooth, lubricated surface for articulation of the bones, together with the lubricating synovial fluid and facilitates the transmission of load with low friction coefficient [14, 16]. Articular cartilage also sustains great dynamics and static forces between articulating bones. In this regard, articular cartilage injuries jeopardize the correct mechanical function of the joint, exposing the articulating surfaces to mechanical overload. This overloading can potentially initiate further tissue damage. Thus, the preservation and health of articular cartilage is important for joint health also due to limited capacity for intrinsic healing and repair of articular cartilage.

2.1 Structure and Function

Articular cartilage is in human a 2 to 3 mm thick porous viscoelastic fiber reinforced tissue [17]. Cartilage tissue is referred as biphasic material, composed of a solid phase and a fluid phase [18]. The main components of the solid phase are collagen (15-22% of wet weight (w. w.) [14]) and PGs (4-7% of w. w. [14]). The fluid phase consists of interstitial water (60-80% of w. w. [19]) and electrolytes. Together the two phases form the extracellular matrix (ECM) which surrounds the cartilage cells, chondrocytes.

Articular cartilage can also be divided into three zones based on the composition and structure of the cartilage in different depths [20]. The zones are the superficial zone, the middle zone, and the deep zone (Fig. 2.1) [16]. The superficial zone is responsible for most of the tensile properties of cartilage, enabling it to resist the sheer, tensile, and compressive forces imposed by articulation. The middle zone provides an anatomic and functional bridge between the superficial and deep zones, and it is the first line of resistance to compressive forces. Finally, the deep zone gives cartilage its greatest resistance for compressive forces since the collagen fibers in the deep zone are arranged perpendicular to the articular surface.

Cartilage under the deep zone is called calcified cartilage. It plays an important role in securing the cartilage to bone by attaching the collagen fibers of the deep zone to subchondral bone as shown in Fig. 2.1. Moreover, the cell population is scarce and chondrocytes are hypertrophic in calcified cartilage.

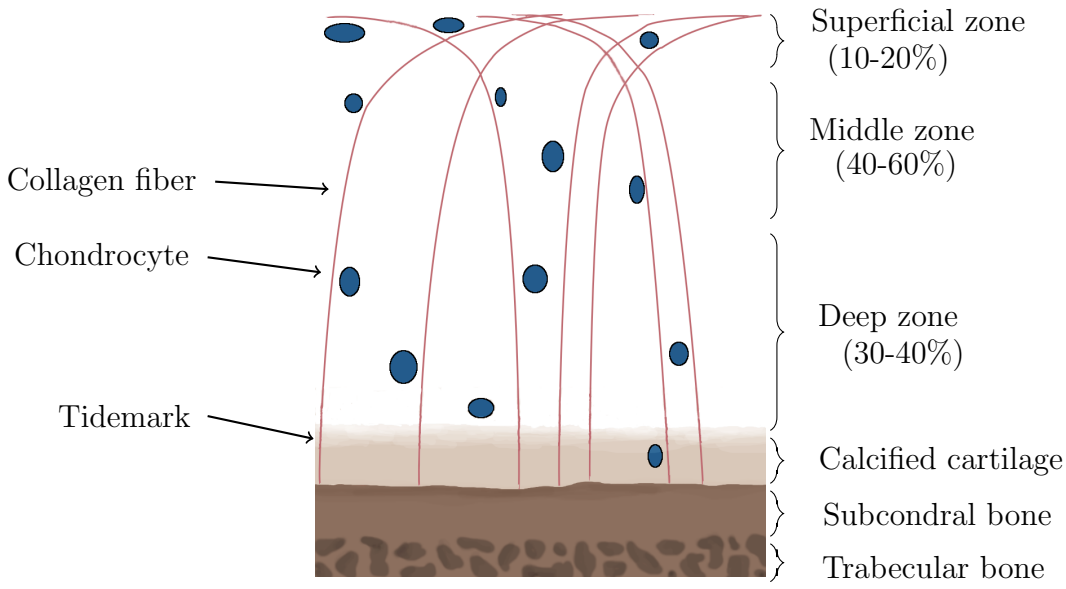

Figure 2.1: A schematic illustration of articular cartilage. The collagens are oriented parallel to the articular surface in the superficial zone, while in the middle zone the orientation is more random. In the deep zone, the orientation is perpendicular to the cartilage-subchondral bone interface. The tidemark represents the calcified-noncalcified cartilage interface.

Collagen fibers (primarily, type II collagen) form the internal skeleton of articular cartilage. They are tightly packed, aligned to the articular surface, and extensively cross-linked. This unique structure gives cartilage its high tensile strength and shear stiffness [21, 22]. The preferential direction of the collagen varies between the cartilage zones. In the superficial zone, the fibers are oriented in parallel to the surface and are densely packed. In the middle zone, the fibers are oriented more randomly but they start to orient in a more perpendicular manner to the surface. Furthermore, in the deep zone, the fibres are arranged perpendicular to the articular surface and the fibers are attached to the bone through the calcified cartilage [19,23]. Additionally, to these zones, secondary collagen fibers are oriented randomly throughout the cartilage. The collagen concentration decreases from the deep zone to the middle zone and then increases again towards the surface [24].

PGs are proteins that are heavily glycosylated [25]. A PG monomer consist of a core protein with one or more covalently bound glycosaminoglygan (GAG) chains. GAG molecules are negatively charged due to their carboxyl and sulphate groups, providing a negative fixed charge for the tissue [26]. This fixed charge inflicts imbalance in osmotic pressure in the extracellular matrix. Consequently, water is drawn into the extracellular space, causing the swelling of the tissue. This swelling is, however, compensated by the collagen network of the cartilage resulting in swelling pressure. Swelling pressure affects significantly to the mechanical properties of the

cartilage, primarily to its compressive stiffness [14]. The PG concentration is highest in the deep zone decreasing towards the cartilage surface [14, 27].

Cartilage cells, chondrocytes, are highly differentiated cells that rely mainly on anaerobic metabolism [28]. Healthy articular cartilage has only 1-5% of its volume chondrocytes [23]. Chondrocytes attend to assembling and synthesis of cartilaginous matrix components and their distribution within the tissue. Moreover, chondrocytes can react to changes in the ECM by modifying the balance between anabolic and catabolic reactions and by replacing the lost macromolecules due to tissue degeneration [29]. The activity of the chondrocytes decreases over time [30]. The activity to synthesize collagen and PG also depends on the mechanical and physiochemical properties of the environment [19].

In addition to providing lubrication, water maintains the transportation of nutrients and ions across the articular surface to chondrocytes. Water can freely move in and out from cartilage but a part of it is bound to the collagen fibers. The transportation of water occurs through diffusion and convection owing to the avascular structure of the cartilage. The flow of water affects the mechanical properties of the tissue. Water contains also a high concentration of cations to balance the negative fixed charge density caused by PGs. The water concentration is the highest in the superficial zone and the lowest in the deep zone [19].

Joint motion and load are important for maintaining the normal articular cartilage structure and function. Inactivity of the joint can cause degeneration of the cartilage [19]. There are two main mechanisms that ensure the minimal friction between articulating surfaces. Firstly, macromolecules, such as lubricin, in the synovial fluid lubricate the surfaces [31]. Secondly, the interstitial fluid pressurizes during dynamical loading, thus forming a thin fluid film in the articulating surfaces decreasing the friction [32]. Cartilage tissue can efficiently adapt itself to the prevailing loading conditions owing to its porous and viscoelastic nature. During the mechanical loading, the collagen network and increasing fluid pressure inside the cartilage control the deformation by stiffening the cartilage. In static loading, cartilage softens while water flows within and out from the cartilage enabling the loading to distribute to the larger contact area.

Articular cartilage lacks blood vessels, lymphatics, or nerves [14]. Thus, the synovial fluid functions as the main source of nutrition for cartilage. The absence of blood vessels, lymphatics, and nerves is also the main reason for the slow regeneration of articular cartilage especially after mechanical injury. The unique and complex structure of articular cartilage complicates the effective treatment and repair.

2.2 Cartilage Injuries, Clinical Diagnostics and Treatment

Articular cartilage injuries of a knee are relatively common [33]. Damage to articular cartilage is called a chondral injury or, if the underlying bone is also fractured, an osteochondral injury [34]. Usually, a damage is a result of an accidental injury, such as a fall, a sport injury, or any other source of a physical trauma. Acute lesions caused by trauma, indirect impact loading, or torsional loading of a joint are especially common in young, athletic adults. A injury of articular cartilage can result in joint pain, swelling, loss of mobility, increased amount of synovial fluid, and local tenderness in the injured area during the compression. Furthermore, other joint injuries, such as meniscal lesions, often cause dominant symptoms as compared to cartilage lesions. A articular cartilage injury can also initiate PTOA [35, 36]. PTOA is a type of joint disease in which articular cartilage degenerates gradually and eventually depletes.

Due to limited capacity for self-repair, a focal damage can eventually lead to complete degradation of the tissue. Thus, for effective treatment of the injury and prevention of PTOA, early diagnostics of fresh cartilage degeneration is important. Nevertheless, with the current diagnostic techniques that include MRI, clinical examination, native X-ray imaging, and arthroscopic examination, the detection of cartilage degeneration is difficult or even infeasible since they can only detect late and major tissue changes. For example, in MRI the resolution is limited and the queuing times in hospitals are long while in native X-ray imaging cartilage is unvisible since the attenuation of the cartilage and the surrounding soft tissue are similar. However, contrast agent-based CT provides a promising tool for identifying fresh cartilage injuries. CECT of a knee joint can be performed with a conical X-ray beam to acquire images covering a large volume with a single rotation around the knee. CECT imaging of a knee joint can be conducted using CBCT shown in Fig. 2.2(a). As the natural contrast between the synovial fluid and cartilage on a native X-ray is almost indistinguishable, in CECT contrast agents are used to enhance the interface of the synovial fluid and cartilage.

The earliest signs of cartilage damage are loss of PGs [38] and disruption of the superficial collagen network [39,40]. They increase the permeability of tissue, thereby affecting the diffusion of the contrast agent into articular cartilage [41, 42]. Thus, fresh cartilage injuries can be detected by observing the changes in contrast agent diffusion with the use of CECT [10, 11]. Currently, two images are usually acquired for the CECT of a knee joint: immediately after and at 45 minutes after contrast agent injection into the synovial fluid. The first image (Fig. 2.2(b)(A)) is required in segmentation of the cartilage as the contrast at the articular surface decreases due to contrast agent diffusion into cartilage. Delayed imaging (Fig. 2.2(b)(B)) is

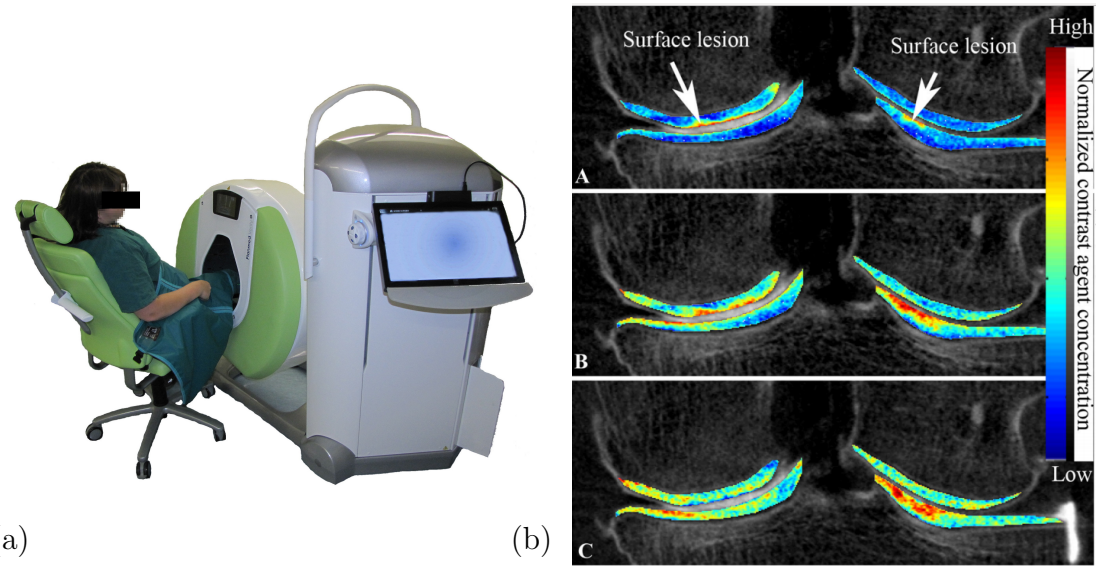

(a) (b)

Figure 2.2: (a) A modern peripheral CBCT scanner (Verity, Planmed Oy, Helsinki) optimized for orthopedic imaging. (b) (A) Arthrographic images are acquired immediately after the contrast agent injection highlighting the cartilage lesions. (B) Delayed images acquired 45 minutes after the contrast agent injection, in addition to cartilage lesions, highlighting also inferior cartilage integrity around the original lesion. (C) Images depicting difference between the delayed and arthrographic images (i.e. contrast agent diffusion). Detecting initiation of PTAO is possible based on these images. [37]

conducted usually at 45 minutes after administration since the maximum contrast agent concentration in the cartilage is achieved at 30–60 minutes after the injection, depending on the location in the joint and the contrast agent efflux from the knee joint [37]. Delayed imaging is needed for the detection of cartilage injuries as the contrast agent concentration at the injured or degenerated site elevates more as compared to healthy tissue. Detecting PTOA is possible by depicting the differences between the delayed and arthrographic images (Fig. 2.2(b)(C)).

If the cartilage injury is detected early enough, the development of PTOA could be prevented by interventions since the cartilage lacks the ability to heal by itself. With the current treatment of significant joint injuries, the risk of PTOA varies from about 20% to 50% [43]. Surgical interventions to repair cartilage injuries by stimulating the growth of new cartilage have evolved during the past years. Bone marrow stimulation is the most commonly used surgical technique to repair cartilage injuries [44]. In bone marrow stimulation, multiple holes are made to the subchondral bone plate so that the bone cells can enter from the bone marrow into to cartilage lesion. These cells are then able to differentiate into fibrochondrocytes. Fibrochondrocytes posses features of fibroblasts and chondrocytes; fibroblasts produce collagen I such as fibroblasts and have a similar rounded morphology protected by a territorial matrix as chondrocytes

Surgical interventions also include autologous chondrocyte transplantation [45] and autologous osteochondral mosaicplasty [46]. Autologous chondrocyte transplantation is conducted in three stages to restore the hyaline cartilage at the repair site. In the first stage, cartilage samples are harvested arthroscopically from a less weight bearing area. Then, cartilage cells are grown *in vitro* and finally injected into the lesion under a periosteal flap sutured to cartilage to cover the lesion. A autologous osteochondral mosaicplasty requires only one operation. The operation involves obtaining multiple small cylindrical osteochondral grafts from a less weight bearing area and transplanting them into the cartilage lesion. In addition to surgical intervention, pharmaceutical interventions can be used to prevent the development of PTOA [4, 5].

3. CONTRAST ENHANCED COMPUTED TOMOGRAPHY

In this chapter the concepts of CECT of articular cartilage are discussed. The chapter is began by introducing the basics of X-ray CT. Then, the contrast agents used to highlight specific structures in the joint are introduced and moreover, the physics of contrast agent diffusion into cartilage is described. Finally, we review the basic idea behind CECT.

3.1 X-ray Computed Tomography

X-ray CT is an imaging technique used in medicine, as well as industrial applications, for visualizing interior features within solid objects and for obtaining 3D images to study their geometries and properties [47, 48]. Tomography refers to a technique in which imaging is done in sections or by sectioning through the use of penetrating waves such as X-rays. The concepts of X-ray CT are discussed in this section based on the references [49–51] unless mentioned otherwise.

X-radiation
X-radiation, is a form of electromagnetic radiation composed of X-rays with the wavelength of 0.01 to 10 nanometers and energies varying from 100 eV to 100 keV. X-radiation is harmful for living cells because high-energy X-ray photons are able to ionize atoms and disrupt molecular bonds. A extremely high radiation dose received in a short amount of time causes radiation sickness while a lower doses increases the risk of radiation-related cancers. Nevertheless, cancer treatments are based on the ionizing capability of X-rays and their capability to kill malignant cells.

X-rays with high energies (5-10 keV) are called hard X-rays, while X-rays with lower energy are called soft X-rays [52]. Since soft X-rays have low energy they are easily absorbed by air and by other mediums. Hard X-rays, on the other hand, can traverse relatively thick objects without being much absorbed or scattered; therefore, hard X-rays are widely used in imaging, e.g. in medical radiography or in industrial radiography.

Production
X-rays are produced in an X-ray tube by accelerating electrons with a high voltage

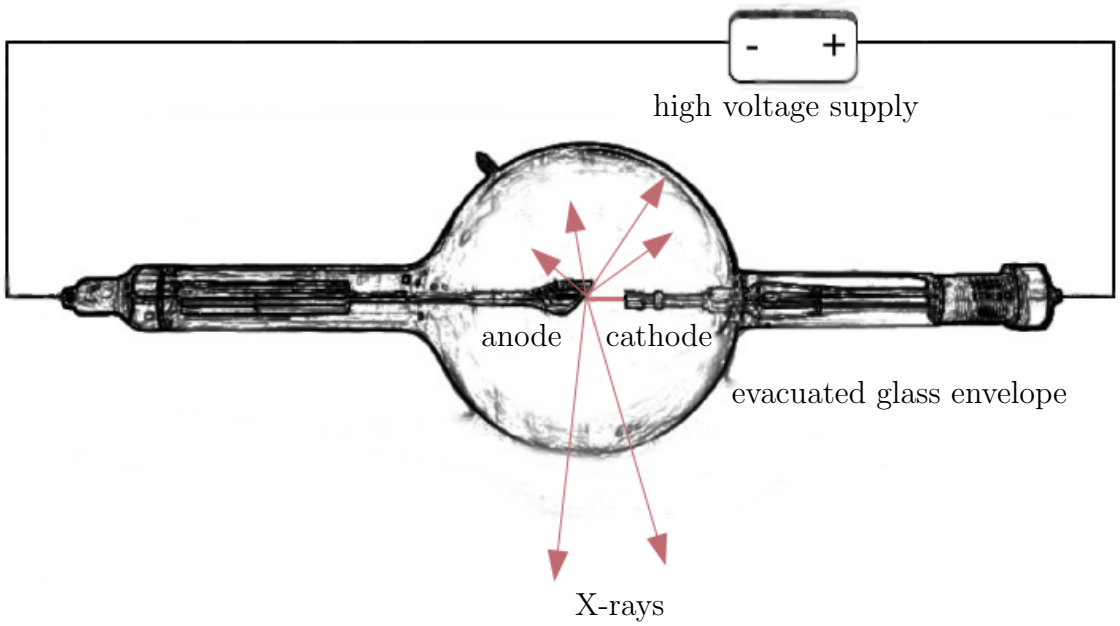

Figure 3.1: A schematic representation of an X-ray tube. In the X-ray tube, the electron beam is generated by heating the cathode. The electron beam is rapidly accelerated with a high voltage against the anode in vacuum, and upon colliding with the anode, a beam of X-rays is generated and emitted throught the window designed for escape of the generated X-ray photons.

and allowing them to collide with a metal target. Fig. 3.1 shows a schematic representation of an X-ray tube. In the X-ray tube, thermionic emission causes the release of electrons when the cathode is heated. The emitted electrons are accelerated by a high voltage towards the anode, which is positively charged relative to the cathode. Operating acceleration voltages of modern clinical CT scanners vary among different scanners but generally fall between 80 and 150 kVp. Here, peak kilovoltage (kVp) refers to the maximum voltage applied across an X-ray tube determining the kinetic energy of the accelerated electrons in the X-ray tube and the peak energy of the X-ray emission spectrum. The electrons accelerated by this high voltage are referred to as projectile electrons. A vacuum is required inside the X-ray tube to prevent the projectile electrons from interacting with the air molecules. Without vacuum, the projectile electrons will loose their energy in collisions before reaching the anode.

Two types of X-rays are created when the projectile electrons hit the anode. Brehmsstrahlung X-rays or ”braking radiation” are released when the accelerated projectile electrons hit the anode and decelerate as they collide with the electrons in the metal. As the projectile electrons decelerate, they lose their kinetic energy which is converted to electromagnetic radiation, in this case, to X-rays with wavelengths between 0.01 and 10 nm. The closeness of approach of the projectile electron to

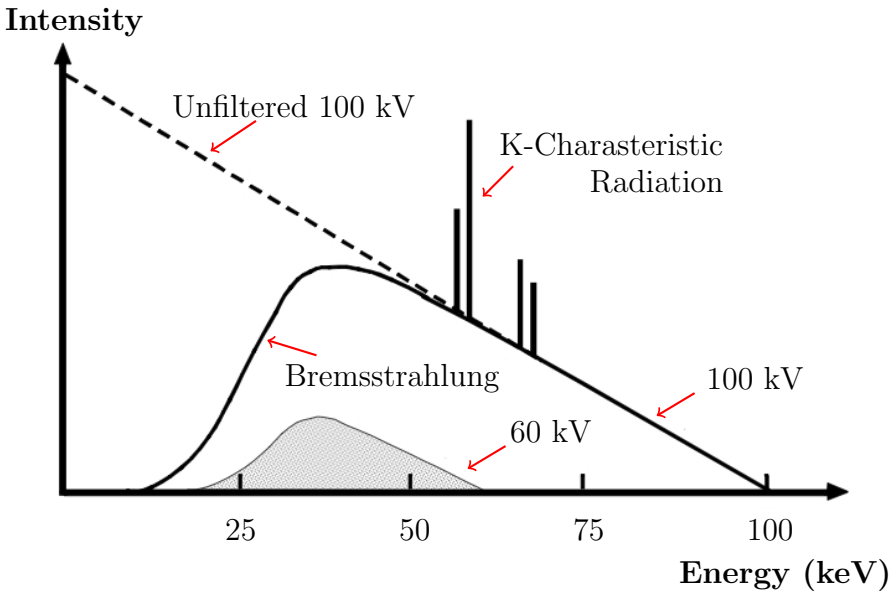

Figure 3.2: The X-ray energy spectrum. The effect of filtering can be seen as loss of low energy photons. Modified from [53].

the target nucleus affects the amount of energy radiated. Thus, the energy of the brehmsstrahlung X-rays vary from 0 up to maximum energy equal to the energy of the projectile electrons which numerically corresponds the accelerating electrical potential.

The other type of X-rays produced in an X-ray tube are characteristic X-rays. They are created as the bombarding projectile electrons with sufficient energy excite an electron of a target metal atom. When the electrons from higher states fill the vacancies, X-ray photons are emitted with precise energies determined by the electron energy levels. As a result of different electron energy levels in metal atoms of which the electrons of a target metals atoms can excite, characteristic X-rays are monoenergetic. The X-ray energy spectrum generated by the X-ray tube is presented in Fig. 3.2.

Generally, projectile electrons never lose their energy in one interaction. Projectile electrons collide with multiple atoms in the anode; therefore, due to these collisions only one percent of the electron beam energy is converted to photons while the rest is converted to heat. To get rid of the heat, a large anode can be used to absorb the heat but this mechanism is based on the conduction in the metal anode. Typically, the conduction in the anode is excessively slow resulting in melting of the anode material. To avoid melting, the anode is rotated, thus continuously exposing a new surface to the electron beam and enabling the rest of the anode to cool down before it rotates back to the position of the beam of electrons.

Clinical CT scanner

A clinical CT scanner consists of an X-ray tube and a detector that are diametrically attached to a big turning gantry which can spin around a patient. During the scan, the patient is lying on a table that is attached to the CT scanner and moving trough the gantry while the gantry is rotating around the patient. This allows X-rays pass through the patient in different angles so that each rotation of the gantry yields several images of thin slices of the patients' body. The time needed for the scan varies between different types of the scan; however, most scans are completed in ten to fifteen seconds. After the scan, computer reconstructs a detailed image of structures inside the body.

X-ray attenuation and interaction with matter

X-ray image is created as a X-ray beam passes through the body section projecting an image onto a detector. X-ray imaging is based on the variable attenuation of X-rays in different tissues. Attenuation is the reduction of the intensity of an X-ray travelling in medium. Attenuation of the X-ray depends on the penetrating characteristics of the beam and the physical properties of the tissues. As an electromagnetic radiation and by assuming that the X-rays are monoenergetic, X-rays attenuate exponentially by according to the equation:

$$I(x) = I_0 e^{-\mu x}, \tag{3.1}$$

where I is the intensity of the radiation, I_0 the initial intensity of the radiation, μ the linear attenuation coefficient, and x the distance travelled in the medium. A linear attenuation coefficient, on the other hand, describes the fraction of radiation attenuated in a given thickness of a absorber:

$$\mu = \frac{\Delta N}{N \Delta x}, \tag{3.2}$$

where N is the total amount of photons and ΔN the number of photons removed from the X-ray beam in thickness Δx. A linear attenuation coefficient depends on the energy of the radiation, the number of photons traversing the attenuating medium or absorber, atomic number of the absorber, and the electron density of the absorber [54].

In the medium in the diagnostic range below 200 keV, the attenuation is due to three dominate interactions: elastic scattering (Rayleigh scattering), Compton scattering, and photoelectric absorption. Rayleigh scattering is the dispersion of X-radiation by particles that have radius less than approximately tenth the wavelength of the X-radiation. In Rayleigh scattering, the photons interact with the medium and are then re-emitted at the same wavelength in a different direction. Rayleigh

scattering contributes more on very high atomic number (Z) material than for low Z materials [55].

Compton scattering describes an inelastic collision of a photon and a free electron or a loosely bound electron in an outer shell. The collision results in a decreased energy of the photon (Compton effect). The lost energy is transferred to the recoiling electron as kinetic energy. In addition, in inverse Compton scattering, a charged particle transfers part of its energy to a photon. Compton scattering dominates for high energies and low Z.

In photoelectric absorption, a photon interacts with an electron and transfers all of its energy to the electron. The atom to which the electron was bound is ionized, thus producing a photoelectron which is then able to ionize more atoms in its path. The kinetic energy of the ejected electron is dissipated in the material. The vacant electron position will be replaced by other electron from the outer electron orbital, producing either a characteristic photon or an Auger electron with the energy that equals the energy difference of the two orbitals. X-ray spectroscopy or Auger electron spectroscopy utilize these photoelectric effects in elemental detection. As the binding energies in high Z materials are closer to X-ray energies, the electrons in high Z materials are more likely to be involved in photoelectric absorption.

Reconstruction

Once the attenuated X-ray beam have traversed through a patient, it interacts with the detector that measures the number of electrons that have passed the patient, practically the intensity of the attenuated X-ray beam. The most commonly used detectors in CT scanners are scintillator-photodiode solid state detectors. When the X-rays reach the scintillator visible light is produced. This light is then converted to an electric current by the photodiode. Finally, the information is send to the computer which analyses the information received by the X-rays and constructs a image of a slice of a body.

The image is reconstructed mathematically from a large number of one-dimensional projection data acquired at many different angles around the patient. Currently, two types of algorithms are used in reconstructing images: analytical and iterative algorithms [56].

The most commonly used analytical algorithm is the filtered back-projection method. Filtered back-projection is based on a simple back-projection method in which the measured attenuation profiles from different direction are simply projected across the image plane (Fig. 3.3(a)). The resulting image in simple back-projection is a blurred version of the object. In filtered back-projection, the blurriness of the image (start-like artefacts, Fig. 3.3(b)) can be removed by convolving the attenuation profile with a negative wing filter function, illustrated in Fig. 3.3(c), prior to the

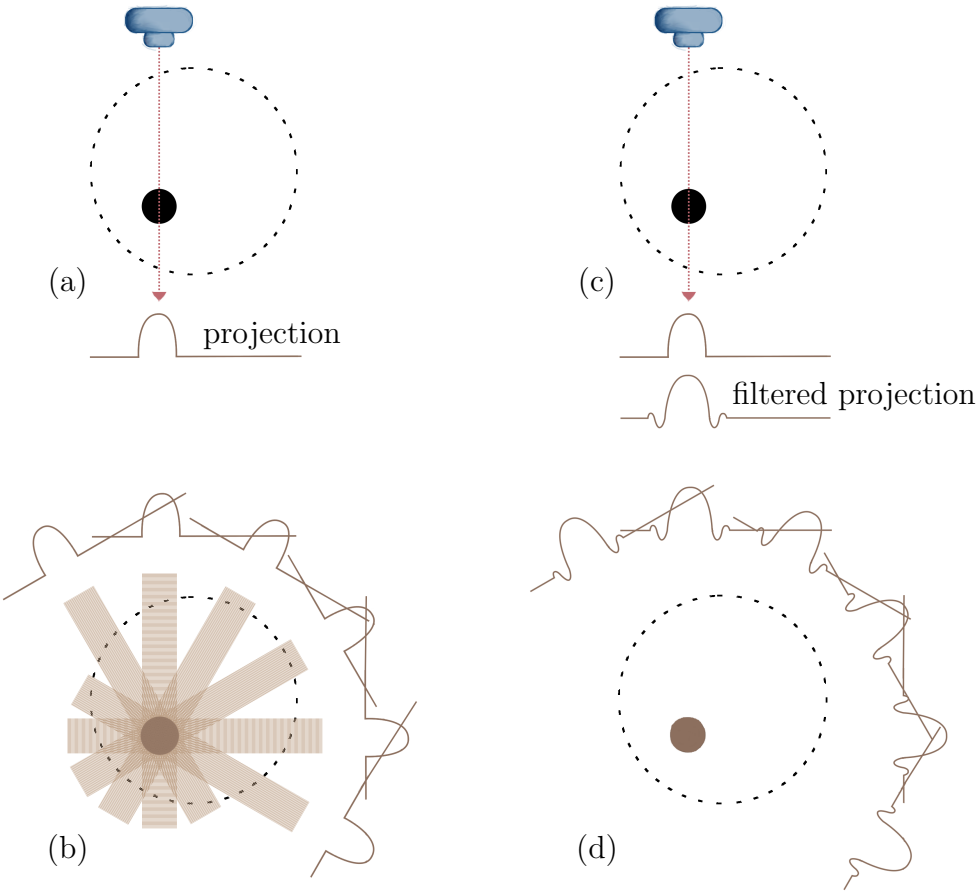

Figure 3.3: An illustration of simple back-projection and filtered back-projection. (a) In simple back-projection, (b) attenuation profiles from different direction are simply projected across the image plane. However, in filtered back-projection, (c) the attenuation profiles are first convolved with a filter function and (d) then back-projected. The illustration is modified from [49].

back-projection. Introducing these negative wings results an accurate representation of the original object (Fig. 3.3(d)). In addition to accuracy of the method, the image reconstruction of the filtered back-projection is fast. Filtered back-projection provides fast image reconstruction since the projections can be preprocessed, filtered, and then back-projected as soon as the first set of measurements are made by the X-ray detectors.

Iterative image reconstruction forms images from projection of an object using iterative algorithms. Iterative image reconstruction is usually considered better but computationally a more expensive alternative to the filtered back-projection method. In iterative image reconstruction, there is a large variety of algorithms available but the basic idea behind the algorithms is the same. First, each algorithm will start

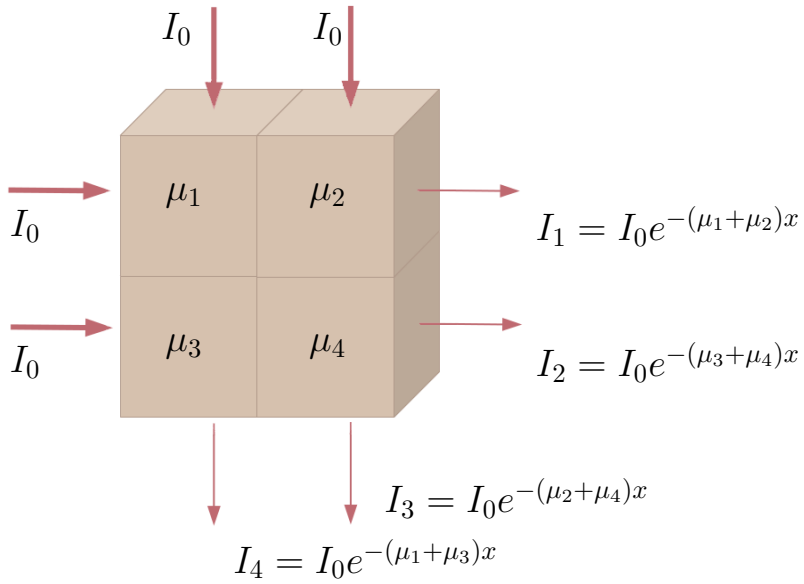

Figure 3.4: A schematic representation of attenuation profiles of voxels.

with an assumed image and computes the projection from that image. Then, the algorithm compares the projection to the original projection data and updates the image based on the differences between the calculated and the actual projections. In that way, the algorithm approaches the correct solution using multiple iterations step by step.

Using one of the reconstruction methods, computer separates the body into small volumes called voxels (3-dimensional pixel). Every organ consists of millions of voxels and each voxel is given a number which represents the extent to which X-rays are attenuated when they pass through the organ. For example, a piece of bone has a very high voxel value because of the strong X-rays attenuation of the bone but for skin the voxel value is low because the skin does not absorb the X-rays as much.

The depth information along the direction of the X-ray beam is lost in radiography but it can be achieved by viewing the slice from many directions. X-ray beam traversing from one side of the patient to another attenuates according to equation (3.1) by all of the voxels through which it passes. Thus, the X-ray beam has an intensity I as follows:

$$I(x) = I_0 e^{-x \sum_{i=1}^{n} \mu_i}, \tag{3.3}$$

where n is the number of a voxel. This equation shows that the X-ray intensity can be expressed as a sum of the attenuation coefficients of the voxels in the path of

X-ray beam, as illustrated in Fig. 3.4. By rearranging this equation as

$$\ln \frac{I_0}{I} = x \sum_{i=1}^{n} \mu_i, \tag{3.4}$$

it is clear that the natural logarithm of the ratio of incident to transmitted X-ray intensities are proportional to the sum of the attenuation coefficients of the voxels in the path of the beam. However, the X-rays produced in the X-ray tube are polyenergic, the equation (3.4) becomes an approximation. Furthermore, beam hardening effect, described later, can lead to an underestimation of the voxel values in the image.

For the image viewing purposes, CT scanner converts the measured attenuation coefficients of the voxels into to CT numbers called Hounsfield units (HUs). Thus, CT number describes the density assigned to a voxel. CT number is a normalized value of the calculated X-ray absorption coefficient so that the density for air is -1000 HU, for water 0 HU, and for compact bone approximately +1000 HU. Most of the human soft tissue have a CT number in the range of -100 – +100 HU. The CT number C_i for a voxel i can be calculated as

$$C_i = 1000 \times \frac{\mu_i - \mu_w}{\mu_w}, \tag{3.5}$$

where μ_i is the attenuation coefficient of the tissue in the voxel and μ_i the attenuation coefficient of water. The scaling factor of 1000 in the equation is used to express the CT numbers in integers. Utilization of integers reduces computer memory and storage requirements.

In this way, a CT scanner can produce a digital image that makes it possible to look at the body in different angles and scroll thought the body to look certain areas. CT images are usually viewed as grayscale images, and the contrast between different tissues can be further enhanced by windowing the image between certain values. Usually, the range of available grey-levels are limited to better correspond the tissue studied rather than allocating the full range of CT numbers. Voxels outside of the selected range, appear either as pure white or pure black.

Artifacts

There are many different kind of artifacts in CT, including noise, beam hardening, scatter, motion, cone beam, helical, ring, partial volume effect, and metal artifacts [57]. Artifacts can obscure the image and, in the worst case, even simulate pathology.

Noise is caused by statistical error of low photon counts. Noise can be seen as random thin bright and dark streaks appearing preferentially along the direction of

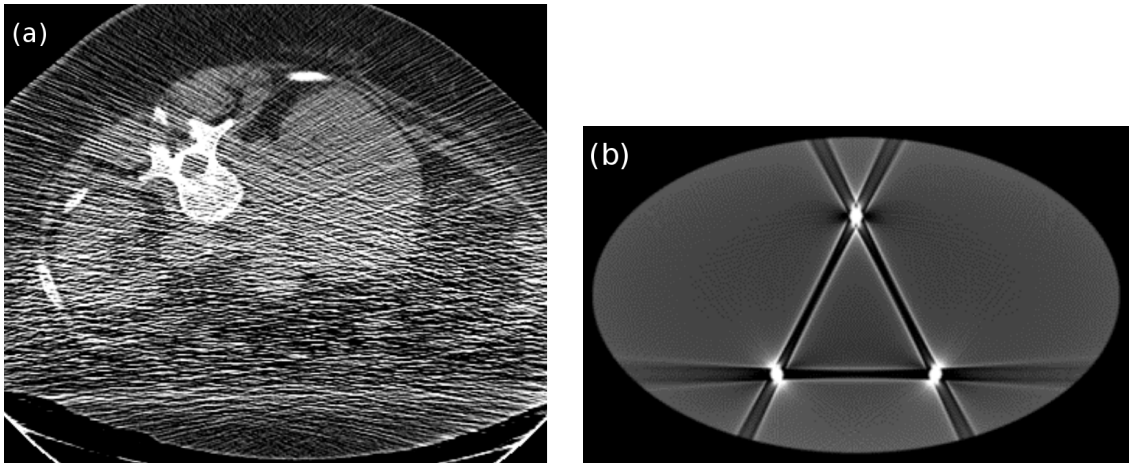

Figure 3.5: (a) A CT-guided biopsy with extensive noise artifact (b) A simulated CT scan showing the beam hardening effect: dark streaks are occuring along the lines of greatest attenuation surrounded by bright streaks in both sides. Figures modified from [57].

the greatest attenuation (Fig. 3.5(a)). Noise affects less on high attenuation objects (e.g. bone) as the boundaries of low attenuation objects (e.g. soft tissue) can be obscured. Iterative reconstruction or performing multiple scans to combine data is used to reduce noise artifacts.

In CT images, beam hardening and scatter appear as dark streaks surrounded by bright streaks adjacent to the dark streak between two high attenuation objects, including bone, metal, and iodinated contrast agents (Fig. 3.5(b)). Beam hardening is observed as an increased high energy photon content in the X-ray beam when the lower energy photons are attenuated more easily as the beam passes through the object. Therefore, unlike monocromatic X-ray, the beam transmission differs from the simple exponential decay. Beam hardening causes the edges of an object to appear brighter than the center despite the material is the same throughout. Compton scatter, on the other hand in the cone beam geometry, obscures CT images by causing the X-ray photons to change direction. In fan beam geometry Compton scattering actually improves the image quality. These photons may then end up in a different detector causing wrong interpretation. Using higher kV causes higher X-ray beam, thus decreasing the beam hardening effect and scatter artifacts. Furthermore, iterative reconstruction reduces both beam hardening and scatter. Beam hardening can also be reduced by using a dual energy CT.

Patient movement, respiration, or cardiac and bowel movements results in blurring, double images, and long range streaks in a CT image (Fig. 3.6(b)). Motion artifacts can be minimized by using a faster acquisition time during which the patient has less time to move. Moreover, some scanners have special features to minimize the artifacts resulting from the motion of the patient.

Helical and cone beam artifacts are related to the scaning geometry. Even though

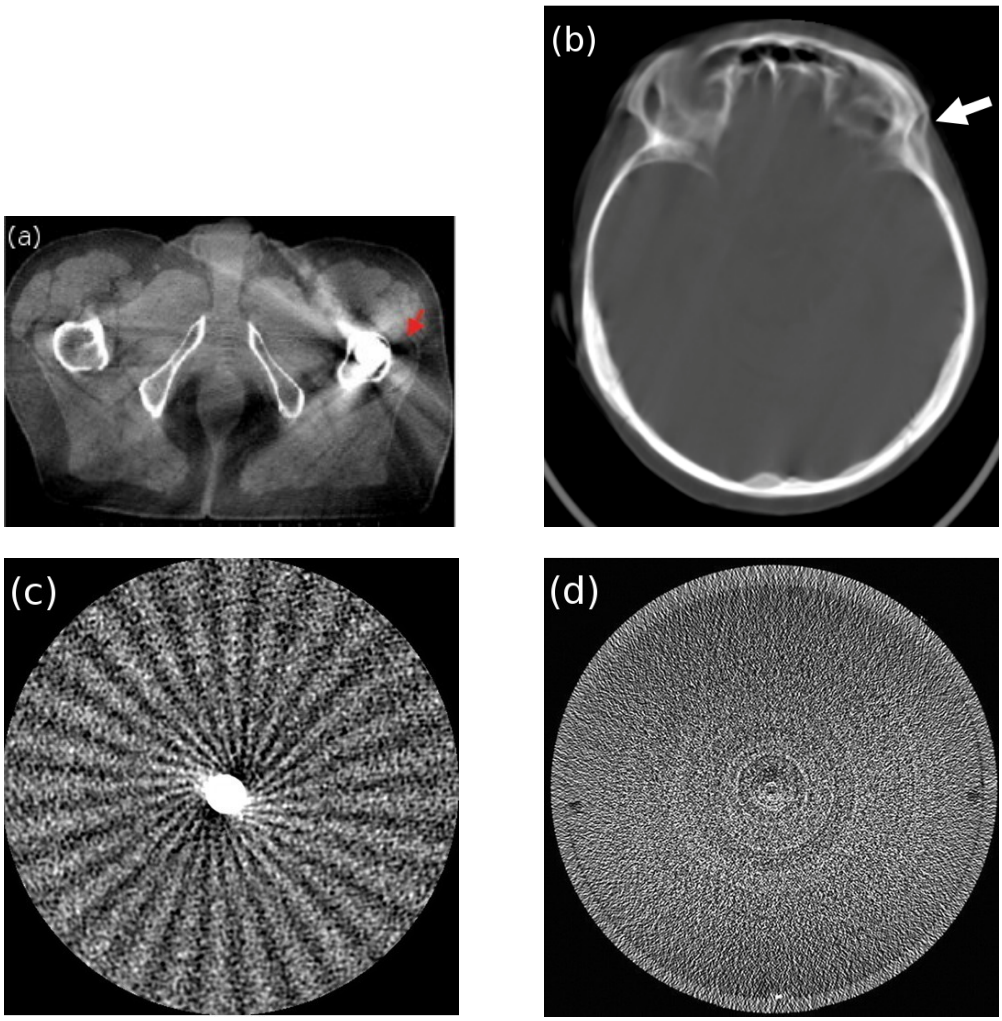

Figure 3.6: (a) A cone beam CT image of prostate patient illustrating the behaviour of streak artifact. Figure modified from [58]. (b) A CT image of the head showing motion artifact, modified from [57]. (c) A simulated CT scan showing illustrating helical artifact, modified from [59]. (d) Ring artifacts around a water-filled phantom, modified from [59].

helical multidetector row and cone beam CTs can reduce artifacts caused by motion, they also have some additional artifacts. For example, as the detector rows in helical CT pass by the axial plane of the object, the reconstruction alternates between conducting measurements from a single detector row and interpolating between two detector rows. Thus, in the case of a high contrast edge between the two detector rows, the interpolated value may be inaccurate. This causes smooth periodic dark and light streaks to form a windmill-like artifacts originated from the high contrast edge (helical artifact). Furthermore, in multidetector row CT, high contrast edges in z direction between the axial plane and the projection plane creates streaks (cone beam artifact (Fig. 3.6(c)). This effects intensifies as the number of detector rows increase. Cone beam artifacts can be reduced by using a Adaptive Multiple Plane Reconstruction (AMPR) [60] or cone-beam reconstructions.

Ring artifacts occur when a detector element is miscalibrated or defective. In CT images, ring artifact appears as rings centered on the center rotation (Fig. 3.6(d)) and can usually be fixed by recalibrating the detector or by replacing it [61]. Ring artifacts are seldom confused with disease, but can impair the diagnostic quality of an image.

Partial volume effect is a combination of two factors: limited resolution of a imaging system and image sampling. Each voxel represents the attenuation properties of a tissue. If that voxel comprises many different tissues, the CT number of that voxel represents some average of their properties. Thus, partial volume effect causing the blurriness of image. Partial volume effect can be reduces using a higher resolution, but this usually prolong the acquisition times. Also partial volume correction is used to minimize the partial volume effect.

Metal artifacts are remarkably common and are due to multiple other artifacts, including beam hardening, scatter, noise, motion, and edge effect related to metal itself or to the metal edges. Metal artifacts are particularly associated with high atomic number metals, such as iron or platinum. Metal artifacts can be avoided by placing the object so that the gantry tilt can angle the metal outside of the axial slices of interest. Iterative reconstruction also helps to reduce metal artifacts.

Image quality control

Filtration is used to reduce the intensity of the X-ray beam, to decrease patient exposure, and to improve image quality for a given radiation dose. The total filtration of the X-ray beam is a mixture of inherent filtration, caused by X-ray tube itself and housing material, and added filtration. Added filtration is a thin sheets of a metal inserted in the X-ray beam. The most commonly used filter materials are copper, aluminium, lead, and brass that are all high atomic number materials. Radiation, emitted by the X-ray tube, is poly-chromatic; thus, filtering helps to reduce the unwanted X-ray energies by removing the long-wavelength X-rays, soft X-rays. Elimination of the soft X-rays reduces the patients' radiation doses since these long-wavelength X-rays are not contributing to the CT image as they absorb fully into patient. The use of filters also produces a cleaner image by absorbing the lower energy X-ray photons that tend to scatter more as compared to higher energy X-rays. Moreover, a more uniform beam improves the image quality by reducing artifacts caused by beam hardening.

Usage of collimators also improve the CT image quality and reduce unnecessary doses to patient. Collimators are located immediately in front of the detectors protecting them from scattered X-rays. Their purpose is to filter the X-ray beam so that only X-ray that are parallel to a specified direction are allowed through. Even though collimators improve resolution, they also hinder incoming radiation by

reducing the intensity and, therefore, also the radiation dose.

X-ray computed tomography devices

CT is one of the most commonly used non-invasive imaging modalities in clinical use due to its wide availability, high efficiency, low cost, and the development of novel hybrid imaging systems. There are many different types of CT devices varying from micrometer-scale preclinical scanner and peripheral quantitative CT (pQCT) to full body instruments with different sampling geometries, as well as dual-energy CT with both single- and dual-source scanners. The sampling geometries include fan beam and cone beam. Spiral CT scanners use a fan-shaped X-ray beam in a helical progression to acquire individual image slices. Here, we will only review the basic idea behind the cone-beam geometry and microCT, used in this study, in more detail.

Cone-beam computed tomography (CBCT) utilizes a divergent pyramidal- or cone-shaped beam to acquire images with a single rotation around the patient. The cone-beam geometry was initially designed as an alternative to conventional CT using either fan-beam or spiral-scan geometries. The advantage of the cone-beam geometry is faster acquisition of a data set and comparatively less expensive radiation detector. In addition, CBCT provides shorter examination time, including the reduction of image distortion due to internal patient movements, and increased X-ray tube efficiency [62]. Compared for example with spiral CT, the advantage of CBCT is its lower radiation doses [63–65]. However, a limitation of image quality related to noise and contrast resolution due to large amounts of scattered radiation detected is a main disadvantage of the cone-beam geometry. CBCT is commonly used in dental imaging because it allows the acquisition of high resolution isotropic image stacks [66].

High resolution microCT is a laboratory equipment that allows the imaging of small objects. It also uses X-rays to generate 3D image of a physical object. It is unsuitable for clinical use. The prefix *micro-* (μ) indicates that the pixel size is in the micrometer range. With microCT, only small objects (diam $<$ 1 cm) can be imaged to obtain the maximal resolution. With larger object sizes, due to applied imaging geometry, the image resolution is reduced.

In microCT imaging, in contrast to the clinical CT, the object is usually rotated while the X-ray source and detector are kept stationary. The cone-shaped X-ray beam is magnified before reaching the detector to create magnified image of the object. This is achieved by placing the object closer to the X-ray source, away from

the detector. The magnification M can be calculated from the equation

$$M = \frac{L^{'}}{L} = \frac{d_{os} + d_{od}}{d_{os}}, \tag{3.6}$$

where $L^{'}$ is the magnified object size, L the original object size, d_{os} the distance between source and object, and d_{od} the distance between the object and the detector.

CT imaging enables the detection of smaller differences in attenuation coefficients; thus, the contrast of CT image is higher compared to a native X-ray image. However, in CT, the maximum resolution is lower than in a native X-ray imaging. The difference of 0.44 % in linear attenuation coefficients can be detected in clinical CT-scanners. Nevertheless, objects less than 0.5 mm apart are difficult to distinguish [67].

Medical uses

Based on the frequency of use and hospital availability, CT is one of the most prevalent diagnostic tools in modern medicine [68, 69]. X-ray CT provides high contrast images with depth information; images can be viewed in the axial, coronal, or sagittal planes, depending on the diagnostic task. Thus, X-ray CT is routinely used in diagnosis in radiology, and moreover, it is a useful tool in radiotherapy treatment planning, prosthesis design, craniofacial reconstruction, stereotactic biopsy planning, and 3D imaging for surgical planning. Furthermore, CT imaging is less expensive, less time consuming, and more readily available compared to other medical imaging technologies such as magnetic resonance imaging (MRI) and positron emission tomography (PET). In clinical use, CT procedure typically takes approximately 30 minutes including the injection of a contrast agent, the positioning of the patient and the imaging. CT can also be used in the detection of fast motion, such as cardiac motion, due to its high temporal resolution [70, 71]. Finally, owing to the development of novel hybrid imaging systems such as PET/CT and single-photon emission tomography (SPECT)/CT, the CT has a great impact on clinical medicine today.

3.2 Contrast Agents

Many tissues can be easily visualized using CT imaging. However, the attenuations of X-ray radiation for different soft tissues, including cartilage, are quite similar. Hence, exogenous contrast imaging agents are used to enhance the contrast and improve the visualization between tissues by increasing the absolute CT attenuation differences between the target tissue and the surrounding tissue as well as fluids [72]. Contrast agents are administered either intravenously or directly injected into the area of interest.

Contrast agents with high Z or high density (ρ) tend to be the best for highlighting desired structures in the body [73]. The relationship can be expressed in the formula for X-ray attenuation coefficient (μ) as follows:

$$\mu = \frac{\rho Z^4}{AE^3}, \tag{3.7}$$

where A is the atomic mass and E the X-ray energy. The reason behind the relation between the high atomic number and attenuation coefficient is photoelectric effect. Photoelectric effect is proportional to the third power of the atomic number of the material (Z^3) and for good contrast images the selection of high atomic number materials is prominent.

In the design of CT contrast agent for clinical application, several requirements need to be considered [73,74]. Firstly, the optimal CT contrast agent should provide maximum imaging capabilities. By increasing the attenuation between the target tissue and its surrounding tissue and fluids at least by a factor of two, contrast agent can drastically improve the visualization of the tissue under examination. Secondly, the contrast agent should be readily transferred to patient. Thus, it should form a stable suspension or be soluble at aqueous physiological conditions e.g. it should have proper pH, osmolality, and low viscosity. Thirdly, the contrast agent should be able to localize the target tissue and posses a favourable biodistribution and pharmacokinetic profiles. Fourthly, the contrast agent and its metabolises should be non-toxic and they should be excreted from the body within the reasonable amount of time (<24 h). However, the retention time of the contrast agent should be long enough for completion of the CT scan (2–4 h) [73]. Finally, the production of CT contrast agent costs should be low and furthermore, the resulting compound should also be stable chemically and as heated.

Iodine-based contrast agents are the most commonly used contrast agents in X-ray imaging due to the high atomic number of iodine ($Z = 53$) [75]. Furthermore, iodinated contrast agents have good solubility and low toxicity due to their functional groups [51]. For example, carboxylic acids and amines attached to the iodinated aromatic ring increase biocompatibility and water solubility of iodinated contrast agents [76]. Furthermore, iodine has a k-edge of 33.2 keV which is suitable for clinical use since the k-edge is close to the mean energy of most diagnostic X-ray beams. K-edge is the binding energy of the K shell electron of a material. The attenuation coefficient of the photons having a energy just above the k-edge increase substantially compared to photons with an enetgy just above the k-edge. Iodine-based contrast agents are usually classified as ionic or non-ionic (organic compound) based on the compound iodine is attached [74]. Ionic contrast agents were developed first but the major disadvantage is that they may result in additional complication

making the introduction of ionic contrast agents difficult for further clinical practice. Despite of this issue, they are still in widespread use depending on the requirements. Non-ionic contrast agents were developed to decrease the possibility of side effects as they covalently bind the iodine and remain undissociated into component molecules. In addition, the advantage of non-ionic over ionic contrast agents is their lower osmolality.

Although iodine-based contrast agents are very convenient in many clinical imaging cravings, the rapid renal clearance restricts imaging applications that require long circulation times. In addition, iodine-based contrast agents sometimes induce serious adverse effects related to the excretion pathway [76]. Lastly, for clinical CT using high-energy X-ray, the attenuation of the iodine is insufficient. To overcome these limitation, nano-sized CT contrast agents have been developed to increase the circulation time and to decrease the undesirable effects.

Recently nano-sized, metallic contrast agents have gained attention as X-ray contrast agents due to their high density and high atomic numbers, thus possessing favourable X-ray attenuation properties [77]. For example, gold nanoparticles (AuNPs) have already been extensively studied as gold provides about 2.7 times greater contrast per unit weight than iodine [78]. Furthermore, AuNPs exhibit low toxicity, facile synthesis, surface functionalization for colloidal stability, and good target delivery [77]. However, AuNPs are expensive and hence the clinical application might cause problems. Thus, in addition to AuNPs, other nanoparticles based on heavy atoms such as lanthanide, tantalum, and bismuth are used as more efficient CT contrast agents.

Inorganic nanoparticles are usually coated by an organic capping layer since nanoparticles are generally unstable owing to their high surface energy and to improve their physicochemical properties. Moreover, nanoparticles also aggregate often due to high ionic strength of many biological fluids [79]. The organic capping layer provides a protective coating, compatible with the solvent, and prevents nanoparticles for aggregating by counteracting the attracting forces occurring between nanoparticles. The coating layer prevents particle surfaces coming into close contact by steric repulsions between the polymer layers. With this separation the van der Waals forces are too weak to cause particles to adhere. TWEEN 80 (polysorbate 80) and polyethylene glycol (PEG) are one of the most commonly used polymers used for coating. In addition to coating polymers, surface of the nanoparticles can be modified to reach certain special features. For example, modification can be used to improve the interactions between the inorganic nanoparticles and the coating polymer [80]. Additionally, the surface can be modified to change the surface charge of the nanoparticle to for example generate a strong repulsion between nanoparticles.

Bismuth nanoparticles (BiNPs) have been studied as a possible contrast agent due

to their high X-ray attenuation coefficient, cost effectiveness, and low toxicity [73]. As compared to iodine, bismuth (Z=83) has greater X-ray attenuation intensity owing to its higher atomic number and electron density. In addition, an inorganic nanoparticle provides many advantages, such as longer circulation and retention times, lower administration volumes, and greater potential for site directed imaging, over more widely used intravascular contrast agents. Bismuth has already been widely used as an ingredient in pharmaceuticals and cosmetics. Furthermore, bismuth(III) salts, such as bismuth oxide, have been used in therapy without showing adverse side effects [13]. As a contrast agent for CT, studies suggest that bismuth-based nanoparticles are efficient dose enhancing agents, and they comprise a great potential in radiotherapy [81].

The challenge of designing new nano-sized contrast agents is the low sensitivity of CT. For example, successful CT requires millimolar concentrations of contrast agents while MRI can detect micromolar concentrations [82]. In typical clinical scanner, the noise level varies from one to three HU; thus, for example a lesion with five to ten HU is detectable. With approximately of 0.5 mg/ml of gold nanoparticles the same contrast can be produced but this concentration is very high compared with many molecular targets expressed in the nanomolar range [83]. Furthermore, most of the nano-sized contrast agents effective for X-ray attenuation have high atomic weights, and most of them are very toxic. Despite these challenges, new nanoparticles have already prolonged circulation times, and the possibility of engineering them for better delivery to target tissue has demonstrated their enormous potential [84, 85].

3.3 Contrast Agent Diffusion in Cartilage

Due to avascular and porous structure of the cartilage, nutrients, and for example contrast agents are transported into cartilage via diffusion [23]. Diffusion is a molecular movement from a region of high concentration to a region of low concentration until the concentration gradient disappears. Diffusion is a dominant form of material transport on sub-micron scales [86]. Diffusion is essentially a question of random fluctuations in the tissue called Brownian motion. Brownian motion is the random movement of the particles in a fluid, thus constantly undergoing small, random fluctuation. The movement of molecules in the cartilage and synovial fluid can be described with Fick's laws of diffusion [87].

The Fick's first law applies only when the system under examination is assumed to be in steady state. The diffusion flux J is the rate of the net movement of the molecules across a unit area, and it is directly proportional to the concentration gradient. The diffusion flux can be expressed according to Fick's first law as follows:

$$J = -D\frac{\partial C}{\partial x}, \tag{3.8}$$

where D is the diffusion coefficient, C the concentration, and x the position along the tissue depth. The diffusion coefficient describes the time needed for a particular solute to move through a particular tissue, and it is a specific constant for the solute of interest and the tissue through which the solute is transported.

The Fick's second law called diffusion law relates the diffusion flux to the concentration when the diffusion flux is time varying. The diffusion flux of contrast agent through the tissue surface in a time dependent case is directly proportional to the concentration gradient, which is always directed towards the lower concentration. The diffusion flux through cartilage surface can be written as

$$\frac{\partial C}{\partial t} = D\frac{\partial^2 C}{\partial x^2}, \tag{3.9}$$

where t is the time. The diffusion flux is always directed towards the lower concentration.

The Gibbs-Donnan equilibrium is a state of equilibrium between two solution containing electrolytes, the ions separated by semi-permeable membrane [86, p. 414]. The distribution of the confined ions in the two solutions cause an electrical potential across the membrane. This potential causes the ions to distribute unevenly across the membrane after the equilibrium for both concentration and electrical charge distribution is reached. At the equilibrium state, Nernst equation gives the ion distribution across the membrane when the gradient of the potential is similar for all the species of the ion. According the Nernst equation, the membrane potential $\Delta\Psi$ can be expressed as

$$\Delta\Psi = -\frac{RT}{zF}\ln\frac{[C]_1}{[C]_2}, \tag{3.10}$$

where R is the gas constant, T the temperature, z the valence of the ion, F Faraday constant, $[C]_1$ the concentration on one side of the membrane, and $[C]_2$ the concentration on the other side. By rearranging this, we get

$$r = \left(\frac{[C]_1}{[C]_2}\right)^{1/z}, \tag{3.11}$$

which is know as a Donnan ratio. Now, the membrane potential can be achieved by combining the Nernst equation and Donnan ratio as

$$\Delta\Psi = -\frac{RT}{F}\ln r. \tag{3.12}$$

This implies that the presence of a fixed charge generates an osmotic gradient across the membrane [88].

To simplify the discussion, three species of small ions Na^+, K^+, and Cl^- are considered with concentrations of c_i. On the side 2 of the membrane, KCl is completely dissolved at concentration C_2, and on the side 1, NaR is completely dissolved at concentration C_1. Here, R^- refers to a generic non-mobile ion which is unable to move from other side of the membrane to other. If some Na^+ are imported to the other side of the membrane, at the same time some K^+ need to be expelled or some CL^- imported as electronegativity must remain unchanged. Thus, one can state that $z = x - y$. Using the equation 3.11, the following group of equations can be formed as

$$\frac{c_{1,Na^+}}{c_{2,Na^+}} = \frac{c_{1,K^+}}{c_{2,K^+}} = \frac{c_{2,Cl^-}}{c_{1,Cl^-}} \Rightarrow \frac{C_1 - (x-y)_1}{x - y_2} = \frac{x_1}{C_2 - x_2} = \frac{C_2 - y_2}{y_1}. \tag{3.13}$$

By reducing this to $x + y = c_2$ and by solving the equatin in term of x, y and z, we get

$$x = \frac{(C_1 + C_2)C_2}{C_1 + 2C_2}, \quad y = \frac{C_2^2}{C_1 + 2C_2}, \quad z = \frac{C_1 C_2}{C_1 + 2C_2}. \tag{3.14}$$

Finally, the Donnan ratio can be presented as Gibbs-Donnan relations:

$$\frac{c_{1,Na^+}}{c_{2,Na^+}} = \frac{c_{1,K^+}}{c_{2,K^+}} = \frac{c_{2,Cl^-}}{c_{1,Cl^-}} \qquad \text{in equilibrium.} \tag{3.15}$$

Now, it is clear that the fixed charge on one side of the membrane distributes the mobile ions unevenly on both sides of the membrane [88]. Finally, the Donnan ratio r can be presented as

$$r = \frac{[Na^+]_1}{[Na^+]_2} = \frac{[K^+]_1}{[K^+]_2} = \frac{[Cl^-]_2}{[Cl^-]_1} = \frac{c_1 + c_2}{c_2}. \tag{3.16}$$

The distribution and the concentration of mobile ions in articular cartilage is affected by the fixed charge in the extracellular matrix [89]. Thus, applying above described theory to cartilage tissue, the interactions between mobile ions and fixed charge density can be defined with the Gibbs-Donnan theory [90]. On the other hand, we can assume that the distribution of mobile ion can be expressed using Donnan equilibrium (eq. 3.16) since negatively charged GAG-molecules are effectively bound to the extracellular matrix. Now, assuming ideal Donnan conditions and taking the charge of the ions into account, the equilibrium in cartilage can be written as [91]

$$\left(\frac{[\text{cation}]_{\text{bath}}}{[\text{cation}]_{\text{cartilage}}}\right)^{z_{\text{cation}}} = \left(\frac{[\text{anion}]_{\text{bath}}}{[\text{anion}]_{\text{cartilage}}}\right)^{z_{\text{anion}}}. \tag{3.17}$$

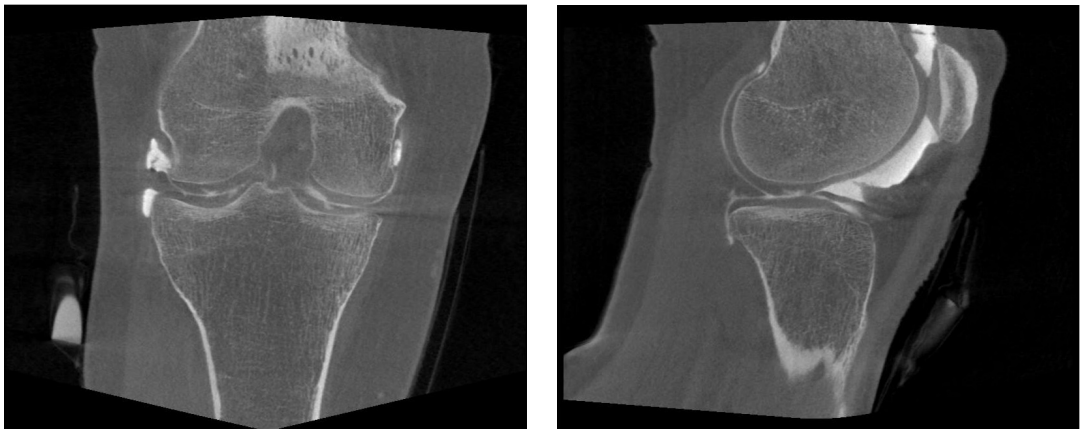

(a) Coronal view (b) Sagittal view

Figure 3.7: CECT image of a knee immediately after the contrast agent administration. Left-hand image is showing the knee in front (coronal) while right-hand image is from the side (sagittal). Injected contrast agent is the brightest area in the picture highlighting the synovial fluid.

Here, it is good to notice that cartilage is assumed to be externally electroneutral, and thus

$$z_{\text{cation}} \cdot c_{\text{cation}}^{\text{cartilage}} = z_{\text{anion}} \cdot c_{\text{anion}}^{\text{cartilage}} + \text{FCD}, \tag{3.18}$$

where FCD refers to fixed charge density of the cartilage caused by GAG-molecules [26].

The structural and compositional features of the cartilage affect the contrast agent diffusion. The diffusion coefficient varies between the different layers of articular cartilage based on collagen and PG concentration as well as the water content. For example, a high collagen content of the deep cartilage is hypothesized to create a steric hindrance to the penetration of the contrast agent [92, 93]. PG content, conversely, may either increase or decrease or may have no affect at all for contrast agent diffusion depending on the contrast agent [94]. Furthermore, the increase in the molecule size decreases the diffusion rate into cartilage [95]. On the other hand, steric interaction between diffusing molecules and cartilage may either increase or decrease the diffusion. Finally, the charge of the contrast agent changes the equilibrium partition; an anion, that has a greater negative charge, has a lower equilibrium partition than an anion with lower charge [96].

3.4 Contrast Enhanced Computed Tomography of the Knee Joint

X-ray arthrography utilizes X-rays to acquire a series of pictures of a joint after injection of a contrast agent, and it has been in clinical use for decades [97–99]. X-ray arthrography allows the detection of superficial lesions as well as the detection of different soft tissue structures of the joint including tendons, ligaments, muscles, car-

tilage, and the joint capsule [100,101]. The visibility of these structures requires the presence of contrast agent since they are invisible on a plain X-ray without contrast agent. Furthermore, the natural contrast between the synovial fluid and cartilage is almost indistinguishable in the knee join. Contrast enhanced computed tomography (CECT) can overcome these limitations. Thus, CECT have been proposed as an effective tool for the detection of lesions in articular cartilage in clinical practice [10].

In CECT examination, contrast agents are used in CT to enhance the contrast between the tissue of interest and the surrounding structures. The CECT imaging of knee joint can be conducted before, immediately after, and at 45 minutes after contrast agent injection to the synovial fluid. The before and immediately after images provide an baseline of the cartilage (Fig. 3.7). Generally, these images are needed for the segmentation of the knee structures from CECT images. The segmentation in later stages of the CECT is impossible with the use of current contrast agents in the market due to their diffusive properties.

Immediately after the contrast agent administration into synovial fluid, the contrast agent starts to diffuse into the articular cartilage. In the iodine-based contrast agent case, the anionic contrast agent distributes in inverse proportion in the cartilage that is negatively charged due to highly negatively charged PGs. Additionally, several *in vitro* studies also suggest high correlation in anionic contrast agent concentration and GAG concentration in cartilage due to diffusion [41, 42, 102–104]. After 30 to 60 minutes from injection, the contrast agents have reached its maximum in the cartilage and owing to this, the interface between the synovial fluid and cartilage is harder to distinguish from the CECT images.

The diffusion of the contrast agent and the equilibrium time, the time required to reach the diffusion equilibrium, depend mainly on the cartilage thickness. The equilibrium time is longer the thicker the cartilage is. In addition to thickness of the cartilage, also the size of the contrast agent affects to the equilibrium time. In the study using the most commonly used contrast agent ioxaglate (Hexabrix, $M = 1269$ g/mol, $q = 1$) the diffusion equilibrium was reached after eight hours [41, 42, 96]. However, when the contrast agent with smaller atomic size (iodine) was used, the equilibrium was observed already after 5 hours [96]. Because the equilibrium takes place after several hours from administration, the equilibrium is unreachable in clinical settings [41, 42, 93].

Despite the long contrast agent equilibrium times, the state of the cartilage can be detected most sensitively before the equilibrium is reached. GAG and contrast agent concentrations correlate already before the equilibrium has been reached [42] allowing the detection of cartilage degeneration and injuries already after 30–60 minutes of diffusion [11]. Thus, so called delayed imaging usually at 45 minutes after administration is required for the detection of OA since the contrast agent

concentration is higher in the degenerated and injured cartilage than in the more intact cartilage [10].

4. MATERIALS AND METHODS

This research project focuses on the development of a novel dual contrast method for delayed CT arthrography of the knee joint. The dual contrast method provides an effective tool for the detection of articular cartilage injuries as well as the detection of the changes in surrounding tissue in clinical practice. Moreover, the method would also reduce the radiation dose significantly as compared to current method used in CECT of the knee joint.

In this chapter, the preparations of the three contrast agents (Hexabrix 15% solution, BiNP suspension, and dual contrast agents) used in this study are described in detail. Furthermore, the protocol for the Z-Average size distribution and the zeta potential measurements of the BiNP suspensions are introduced. The latter part of this section describes the sample preparation along with the sample injuring. Finally, the protocol and analysis of the CECT imaging are explained.

4.1 Contrast Agent Preparations

The planetary milling system (Fig. 4.1) consists of at least one milling jar and a planetary milling device. In contrast agent preparetion, the materials and milling balls are loaded into the jars and placed into the milling device. During the milling process, the jars are rotating around the central axis and simultaneously around their own axes in the opposite direction mimicking the movements of planets around the Sun. The milling balls are subjected to superimposed rotational movements, Coriolis forces. The efficiency of the grinding is the result of the high dynamic energies caused by the difference in speeds between the milling balls as the material particles undergo multiple collisions with the milling balls and the jar walls. Thus, high velocity of moving milling balls create a high stress in the activated material reducing the particle size of the material.

In our study, we measured 170 g of milling balls, 10 g of Bi_2O_3 (202827, nanopowder, 90-210 nm particle size, 99.8% trace metals basis, Sigma-Aldrich), and 30 ml of distilled water for the both milling bowls. Then, the solution was milled for 4 hours using a Planetary Micro Mill Pulverisette 7 (Fritsch GmbH, Rudolstadt, Germany) milling device at a rotation speed of 500 rpm to reach the target particle size. Milling bowls were cooled down after every 15 minutes to ensure that the temperature does not increase excessively. After the milling, BiNP suspension was separated from

(a) The milling jars (b) The milling device

Figure 4.1: The milling system comprises (a) the milling jars and (b) the milling device (Planetary Micro Mill Pulverisette 7, Fritsch GmbH). The yellow powder in the jar on the left side is bismuth oxide and the milling balls are in the jar on the right side.

milling balls using a syringe. Then, 20% of the final volume of TWEEN 80 coating polymer (P1754, viscous liquid, Sigma-Aldrich) was added to produce more stable solution. TWEEN 80 was chosen foe this study since it is safe and well tolerated. Distilled water was added to the suspension to reach the final concentration of 200 mg/ml. Finally, in the preparation of the BiNP suspension, the osmolality was adjusted to the physiological osmolality of 308 mOsm/l [96] using NaCl (7647-14-5, Fisher Chemicals) and the pH of the solutions was adjusted to 7.4 using acetic acid (320099, Sigma-Aldrich).

The dual contrast agent consists of a mixture of two compounds: an iodine-based contrast agent Hexabrix (q= -1, Mallinckrodt Inc., St.Louis, MO, USA) and a suspension of nano-sized bismuth oxide particles coated with positively charged TWEEN 80 surfactant developed by us. The BiNP suspension was prepared similarly as described above. Hexabrix and nanoparticle suspension were transposed so that the mixing ratio was 15% of Hexarix and 85% of BiNP suspension of the final volume. The final concentration of bismuth oxide in the dual contrast agent was 200 mg/ml. Again the suspension was adjusted to the physiological osmolality of 308 mOsm/l and pH was adjusted to 7.4 similarly as mentioned above.

The Hexabrix 15% solution was prepared by mixing Hexabrix with phosphate-buffered saline (PBS, for more details about PBS, see section 4.3.3). In this case, PBS contained only 86.6 mM of NaCl to ensure that the final osmolarity of the

Hexabrix 15% solution remains at the physiological osmolarity of 308 mOsm/l. pH of the PBS solution was adjusted to 7.4 using NaOH. Since Hexabrix is at physiological pH, also the final solution is at physiological pH after the mixing.

Lastly, we prepared an improved BiNP suspension to eliminate the problems detected with the first dual contrast agent. With the improved dual contrast agent (for more detail, see section 5) instead of using TWEEN 80 as a coating polymer, we decided to use polyethylene glycol (PEG). Furthermore, the nanoparticle surfaces were modified. For the improved dual contrast agent, we also decided to reduce the bismuth oxide concentration in the final solution by half because the attenuation of the BiNP suspension was observed to be higher than desired. Thus, the final concentration of bismuth oxide in both the BiNP suspension and the improved dual contrast agent was 100 mg/ml. The BiNP suspension was prepared similarly as described previously. PEG was mixed into the BiNP suspension and stirred until the PEG was completely dissolved. The concentration of the PEG in the BiNP suspension and in the improved dual contrast agent was 25 mg/ml. As the PEG requires heat energy to be able to attach covalently to the hydroxyl groups of the BiNPs, the suspension was heated to 100 °C for 4 hours.

The surfaces of the nanoparticles in the improved dual contrast agent were also modified using citric acid so that the surface charge density was modified from positive to negative. Negative surface charge density keeps the ioxaglate and the nanoparticles from agglomerating due to electrostatic interactions as observed with the first dual contrast agent. The surface modification was achieved by adding 0.06 mg/ml of citric acid (251275, Sigma-Aldrich) to the BiNP suspension prior to PEG insertion into the suspension. The pH of the improved dual contrast agent was adjusted using sodium carbonate (451614, Sigma-Aldrich).

4.2 Analysis of the Bismuth Oxide Nanoparticle Suspension

After the preparation of the BiNP suspension, the size distribution of the nanoparticles and their zeta potential were analysed. Both the size distribution and the zeta potential was measured using a Zetasizer Nano ZS device(Malvern Instruments Ltd, England). This device is using dynamic light scattering for the measurement of particle size and electrophoretic light scattering to measure zeta potential of the particles.

4.2.1 Z-Average size distribution

Z-Average size is a hydrodynamic parameter implying that it is suitable only for particles in a dispersion or molecules in solution. Prior to the size distribution measurement, the concentration was reduced by adding distilled water since high

concentrations are not suitable for the size distribution measurement with Zetasizer Nano ZS device. Then, 3 ml of the sample suspension was measured into a plastic cuvette (FB55143, Fisherbrand) along with 0.15 ml of 5 mM citric acid solution to stabilize the suspension. Ultrasound bath was used to remove any air bubbles in the suspension and to break particle agglomerates because Z-Average size is very sensitive to any changes in the sample, such as a small proportion of aggregates. The size distribution measurement was performed in 25 °C. The count rate was set to be 144.4 kcps and the duration of the measurement to 80 s. The resulting target Z-Average size for BiNPs was set between 100 – 500 nm.

4.2.2 Zeta potential

Zeta potential is the potential difference between the dispersion medium and the stationary fluid layer attached to the dispersed particle. The zeta potential value gives an indication of the suspension stability. A large positive or negative zeta potential signifies that the particles in a suspension repel each other preventing particles from aggregating. Thus in a suspension with a low zeta potential, there are no forces that would prevent the particles from aggregating. Generally, suspensions with a zeta potential below -30 mV or above +30 mV are considered stable, and suspensions with a zeta potential between -30 – +30 unstable. Nevertheless, a suspension that has a particle density different from the dispertant density will eventually sediment. Now, it is also good to note that the zeta potential and surface charge density are not the same but they are related; the zeta potential and the surface charge density are the same when the sample is dispersed into distilled water and is thus at neutral pH.

Also in zeta potential measurement, the samples were dispersed into distilled water to decrease the concentration to more suitable for the measurement. Prior the use, a special zeta potential cuvette (DTS 1070, Malvern) was carefully cleaned in a ultrasound bath with ethanol (99.5%, Altia Oy) and distilled water. Then, the samples were pipetted into a cuvette and air bubbles and particle agglomerates were removed by treating the cuvette and sample in the ultrasound bath. The zeta potential measurements were conducted at room temperature.

4.3 Sample Preparation

Intact bovine knee joints were obtained within 24 hours after slaughtering at a local abattoir (Savo-Karjalan liha Oy, Kuopio, Finland). Then, patellae were carefully dissected from the surrounding tissues. Next, the patellae were wrapped in PBS-soaked gauze and stored in -20 °C. Prior the measurement, patellae were thawed at room temperature.

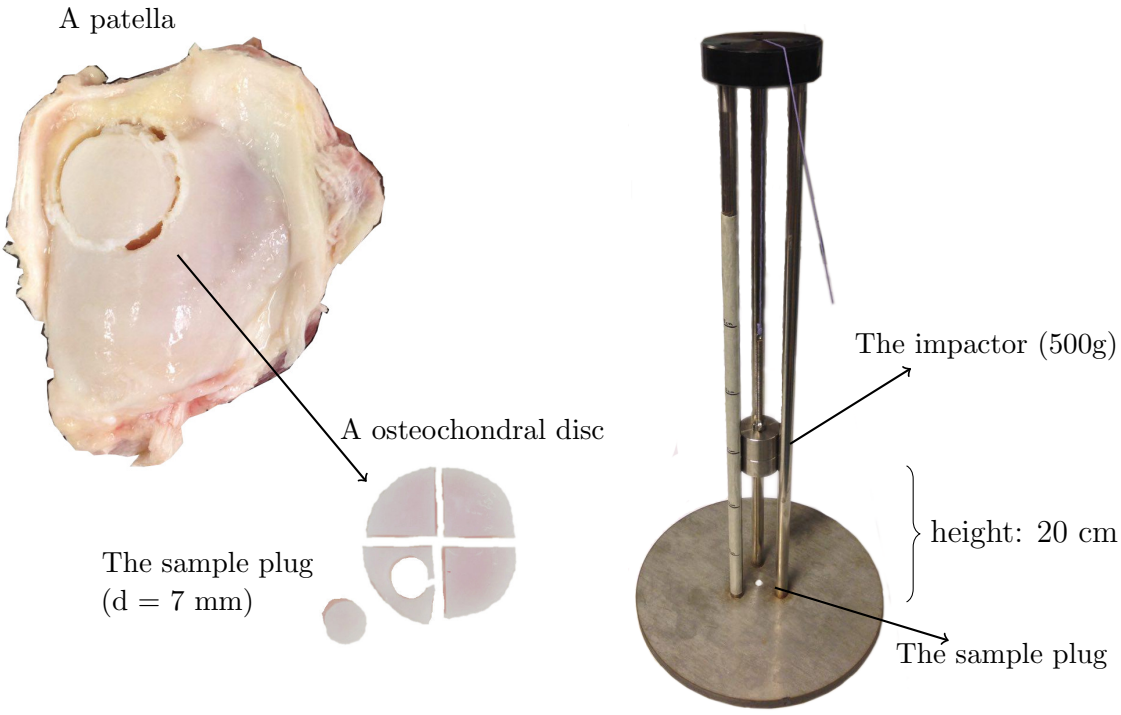

(a) Sample preparation (b) The impact tower

Figure 4.2: (a) The osteochondral disc (d = 2.65 cm) was drilled from the upper lateral part of the patella and the disc was divided into four equal pieces. Then, four osteochondral plugs (d = 7 mm) were punched from each piece and the plugs were trimmed to leave approximately 1 mm of subchondral bone under the cartilage. (b) The custom-made impact tower was used to injure cartilage mechanically. The sample plug was placed in a slot, and the impactor (m = 500 g) was dropped from the height of 20 cm on the sample plug.

After thawing, osteochondral discs (diam. = 2.65 cm) were extracted from the upper lateral part of the patella. Next, four osteochondral plugs were prepared (diam. = 7 mm) by first dividing the disc into four pieces and then, punching smaller osteochondral plugs from each piece (Fig.4.2(a)). Then, osteochondral plugs were trimmed to leave approximately 1 mm of bone underneath the cartilage. After the osteochondral plugs were prepared, two of them were injured. In this study, we created a mechanically induced impact on one osteochondral plug (impact plug B) and trypsin degradation for the other osteochondral plug (degraded plug C). One of the osteochondral plugs served as a backup sample as the remaining osteochondral plug served as a reference sample (reference plug A). These plugs were used in the measurements were nanoparticles were coated with TWEEN 80. An additional degraded plug was prepared similarly as described above for the measurement conducted with PEG. All samples were initially healthy implying that there were no visible surface fibrillation or other early degenerative changes.

4.3.1 Mechanical impact

The samples were injured mechanically using a custom-made drop tower (Fig. 4.2(b)) by dropping a weight of 500 g on the sample from the height of 20 cm, thus the momentum of the weight was 0.387 kgm/s at the moment of impact. The magnitude of the impact was chosen to create minor cracks on the articular surface. This mechanically induced defect corresponds in OA development the characteristic of progressive fibrillation of the cartilage surface [105]. Subsequently, the mechanical injury the sample was immersed in PBS for 2 h at room temperature to prevent any creep deformation.

4.3.2 Enzymatic degradation

Enzymatic degradation treatment can be used to mimic the cartilage condition in early-state OA, including disruption of superficial collagen and PG loss. However, artificial degradation fails to demonstrate all of the complex symptoms of OA, it can only provide some insight into PG loss and collagen disruption [106, 107]. Trypsin is one of the most commonly used enzymes to produce PG depletion [108]. Treating the samples with trypsin, we were able to recreate the characterised signs of early-state OA by degeneration of PGs [109]. Furthermore, trypsin has been shown to also cleave minor amounts of collagen [110]. The degree of degradation can be managed through the concentration of the enzyme solution and the duration of the treatment.

In enzymatic degradation, the samples were digested with trypsin solution (0.5 mg/ml) for 15 hours at 37.5 °C to achieve the specific level of PG depletion. Before digestion, the sample and the trypsin solution were warmed in incubator separately up to 37.5 °C. After the treatment, the samples were immersed in PBS for 2 hours.

4.3.3 Phosphate buffered saline

PBS is a balanced salt solution commonly used in biological laboratories. PBS is isotonic meaning that the osmolarity and ion concentrations of the solutions correspond to that in a human body. Thus, PBS maintains the physiological pH and osmotic balance of the cell along with providing cells with water and essential inorganic ions. PBS can maintain cells suitable environment for the short term while the cells are examined outside of their regular environment.

During preparation, the samples were kept moist with PBS, including 6.4 mM ethylenediaminetetraacetic acid (EDTA) and 6.4 mM benzamide as inhibitors of proteolytic enzymes. PBS is made by dissolving the reagents into the distilled water so that the final concentration of the reagents are as follows: NaCl 137 mM, KCl 2.7 mM, Na_2HPO_4 10 mM, and KH_2PO_4 1.8 mM. The pH of the solution was adjusted to the physiological pH of 7.4 with NaOH.

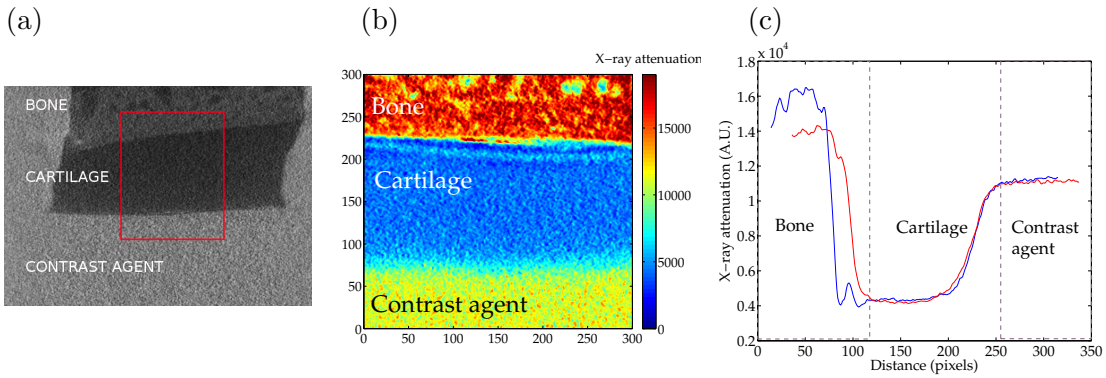

Figure 4.3: (a) A magnified microCT image of a representative sample plug (averaged over 201 consecutive image slices) obtained in this study. The cartilage can be seen in the image as the region which is the darkest. The analysed area is outlined in the picture as red. The width of the analysis area was 2790 μm (201 pixels), and the height was chosen for every sample to leave enough subchondral bone and contrast agent around the cartilage. (b) The magnified image of the analysed area. (c) The X-ray attenuation profile along the vertical direction. The pixel rows are horizontally averaged from the subfigure (b) to obtain the X-ray attenuation profile.

4.4 Contrast Enhanced Computed Tomography Imaging

The imaging was performed for each sample (reference plug A, impact plug B, and degraded plug C) with three different contrast agents (Hexabrix 15% solution, BiNP suspension, and dual contrast agent) using a microCT-instrument (Skyscan 1172, SkyScan, Kontich, Belgium). The imaging order of the contrast agents was selected randomly for every osteochondral plug. The imaging was conducted immediately after the sample plug immersion into the contrast agent and after 45 minutes from the immersion. The tube voltage was 100 kV, the tube current 100 mA, and the isotropic voxel size $13.88 \times 13.88 \times 13.88$ μm^3. The acquisition time for one imaging was approximately 12 minutes. To ensure that the diffusion of the contrast agent occurs only trough the articulating surface, the sides of the osteochondral plugs were sealed with cyanoacrylate. Furthermore, the sample plugs were imaged upside down (i.e. articulating surface towards bottom of the sample tube, as shown in Fig. 4.3 (a)) to the prevent any accrual of the nanoparticles on the surface of the cartilage due to gravitation. After each imaging with different contrast agent, the samples were immersed in an isotonic bath of PBS (60 ml) for two hours at 9 °C to wash out the contrast agent. The time was found to be enough for washing the contrast agent out from the cartilage entirely by imaging the sample plug in PBS with microCT by comparing the baseline image od the cartilage with preliminary tests.

Imaging data was analysed using MATLAB (R2014a, MathWorks, Inc., Natick, MA, USA). At first, microCT image stacks were co-registered for 0-minute and 45-minute time points. Signal-to-noise-ratio was improved by averaging 201 spatially

consecutive coronal slices for both time points. The width of the region of interest (ROI) was selected to be 2790 μm (201 pixels) at the center of the each osteochondral plug (Fig. 4.3(a)). The pixel rows in the ROI were also averaged in the horizontal direction to obtain the depth-wise attenuation profile (Fig. 4.3(c)). The contrast agent diffusion into cartilage was examined by comparing the 0-minute and 45-minute attenuation profiles.

5. RESULTS AND DISCUSSION

The aim of this thesis is to evaluate the feasibility of usage of the dual contrast agents in the detection of the fresh cartilage injuries. To this end, new dual contrasts agent is prepared (see Section 4). In this chapter the properties of the developed dual contrast agent is shown. Also, the initial imaging result using three contrast agents (Hexabrix 15% solution, BiNP suspension, and dual contrast agent (with TWEEN 80 coating polymer)) along with the preliminary microCT imaging results of the improved contrast agent (with PEG coating polymer) are presented. Furthermore, the feasibility of the suggested dual contrast method will be evaluated in the light of current results at the end of this chapter.

5.1 The First Bismuth Oxide Nanoparticle Suspension

Before using new contrast agents in imaging, the properties, such as nanoparticle size and stability, of the prepared solution need to be resolved to evaluate whether the solution is suitable for practical use. For example, if the nanoparticle size is too small, the particles are free to diffuse into cartilage. On the other hand, if the particle size is too large, a nanoparticle size close to 1 μm would cause damage to cartilage *in vivo* as micrometer-sized particles can grind the surface of the cartilage, thus inducing incipient degeneration to the cartilage.

To obtain the size range of the particles in the BiNP suspension, the Z-Average size distribution was measured (see Fig. 5.1 (a)). The mean size of the nano-particles were obtained to be 261.2 nm with the standard deviation of 82.33 nm. Thus, the nanoparticles were large enough to be unable to diffuse into cartilage because the estimated average pore size of cartilage is approximately 6.0 nm [111].

Polydispersity Index (PdI) describes the uniformity of the particles in a suspension in terms of theirs size. PdI is a dimensionless variable calculated from a simple two parameter fit to the correlation data. PdI values smaller than 0.05 are rare and represents highly monodisperse dispersion. Values greater than 0.7, conversely, represents a sample that has a very broad size distribution and is hence unsuitable for the Z-Average size measurement utilising dynamic light scattering technique. In this light, the measured PdI value of 0.171 indicated that the BiNP suspension is relatively monodispersed.

The zeta potential is used to describe the properties of the particles, such as

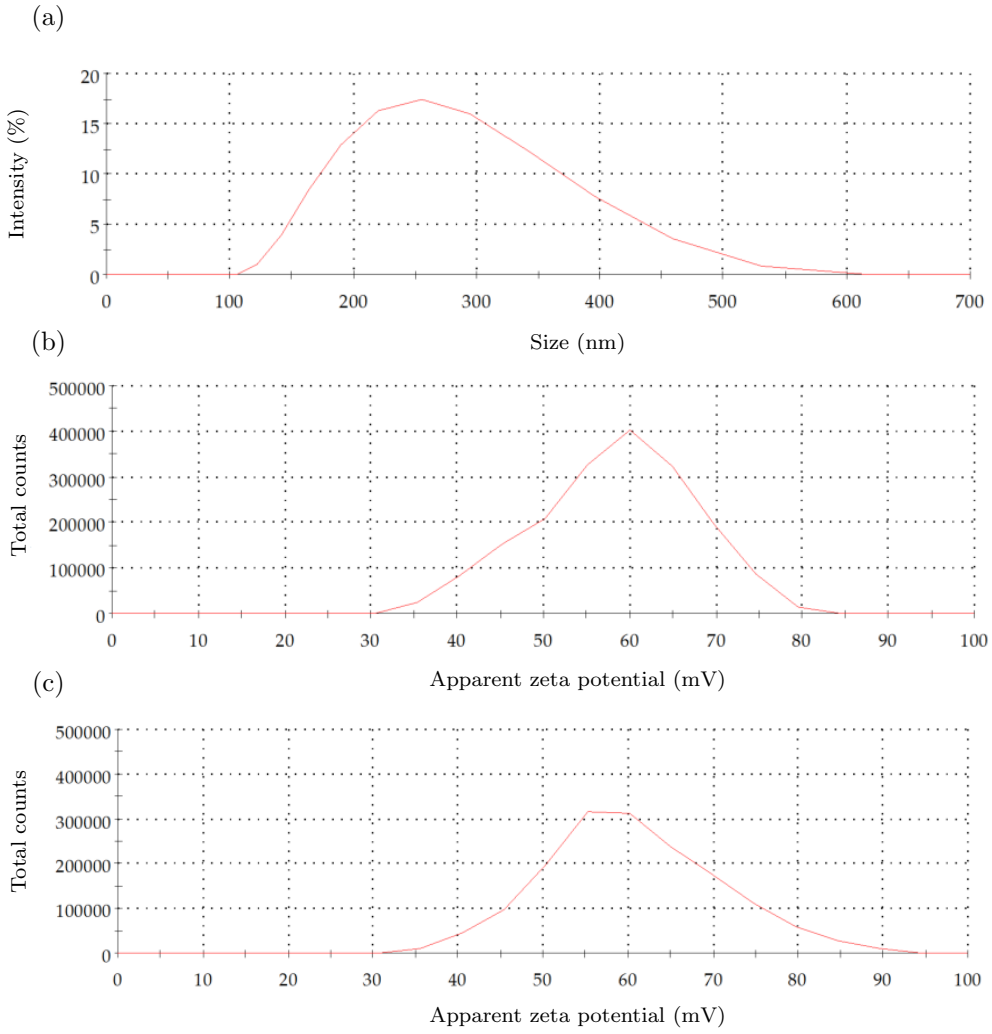

Figure 5.1: (a) Z-Average size distribution of Bi_20_3 nanoparticle suspension by intensity. Average size was measured to be 261.2 ± 82.4 nm and PdI to be 0.171. (b) Zeta potential distribution of Bi_20_3 nanoparticle suspension. Zeta potential was measured to be 58.3 ± 9.3 mV. (c) Zeta potential distribution of Bi_20_3 nanoparticle suspension with TWEEN 80 coating polymer. Zeta potential was measured to be 60.5 ± 10.2 mV.

stability, in a suspension. The obtained zeta potential distributions (see Fig 5.1 (b,c)) of BiNP suspension were obtained to be 58.3 mV and 60.5 mV for suspension without coating polymer and with TWEEN 80, respectively. Thus, both of these suspensions can be considered stable since in general the zeta potential values below -30 mV or above +30 mV are consider to show the stability of the suspension. However, with the particles of this magnitude, the suspensions are settling under gravity with time. TWEEN 80 coating polymer was noticed to slow down the settling of the nanoparticles (data not shown).

5.2 Contrast Enhanced Computed Tomography

The results of this section are divided based on the used dual contrast agent. In the first dual contrast agent, TWEEN 80 was used as a coating polymer while in the improved dual contrast agent the TWEEN 80 was replaced by PEG. Also, the surfaces of the nanoparticles were modified for the improved dual contrast agent.

5.2.1 The First Dual Contrast Agent - MicroCT Images

MicroCT images are a useful and fast way to visually evaluate the condition of the articular cartilage but for more detail X-ray attenuation profiles can be used to provide more detailed information about the condition of the cartilage. The visual evaluation of the microCT images can be done by comparing the images conducted immediately after the contrast agent immersion and 45 minutes after the immersion. Cartilage injuries can be detected by observing the changes in contrast agent diffusion into cartilage as a higher X-ray attenuation.

Hexabrix is one of the most commonly used contrast agent in the CECT, and in this study it will serve as a reference for the dual contrast agent as we compare the ioxaglate diffusion into cartilage. The microCT images of the three samples (the reference plug, the impact plug, and the degraded plug) at 0 minutes and 45 minutes after Hexabrix 15% solution immersion are shown in Fig. 5.2. As can be seen, the contrast agent diffusion into the mechanically injured and enzymatically degraded cartilage is greater than into reference cartilage. Furthermore, the visual detection of cartilage surface changes (such as cracks in the cartilage-contrast agent interface) is challenging or even impossible with Hexabrix 15% solution. However, this might be due to fact that for these images we averaged 201 spatially consecutive coronal slices and thus, the information of the surface changes might have been lost if the changes in the surface were much smaller than the selected ROI.

The contrast at the interface between the contrast agent and cartilage could be retained at high level by implementing nano-sized bismuth nanoparticles. The improved contrast at the cartilage-contrast agent interface would also enable the detection of cartilage surface changes. Thus, to study the potential of nanoparticles, the samples were imaged using BiNPs suspension. The microCT images of all three sample plug at both time points using BiNP suspension are presented in the Fig. 5.3.

Based on our hypothesis, using nano-sized particles, such as bismuth oxide nanoparticles, the contrast of the interface between the cartilage and contrasta agent can be retained at high level, and the changes in cartilage surface could be obtained more clearly. To this end, similar images as shown above were taken by using the BiNP suspension (see Fig. 5.3). It can be seen that the interface between cartilage and surrounding contrast agent remains distinct. This implies that the selected size

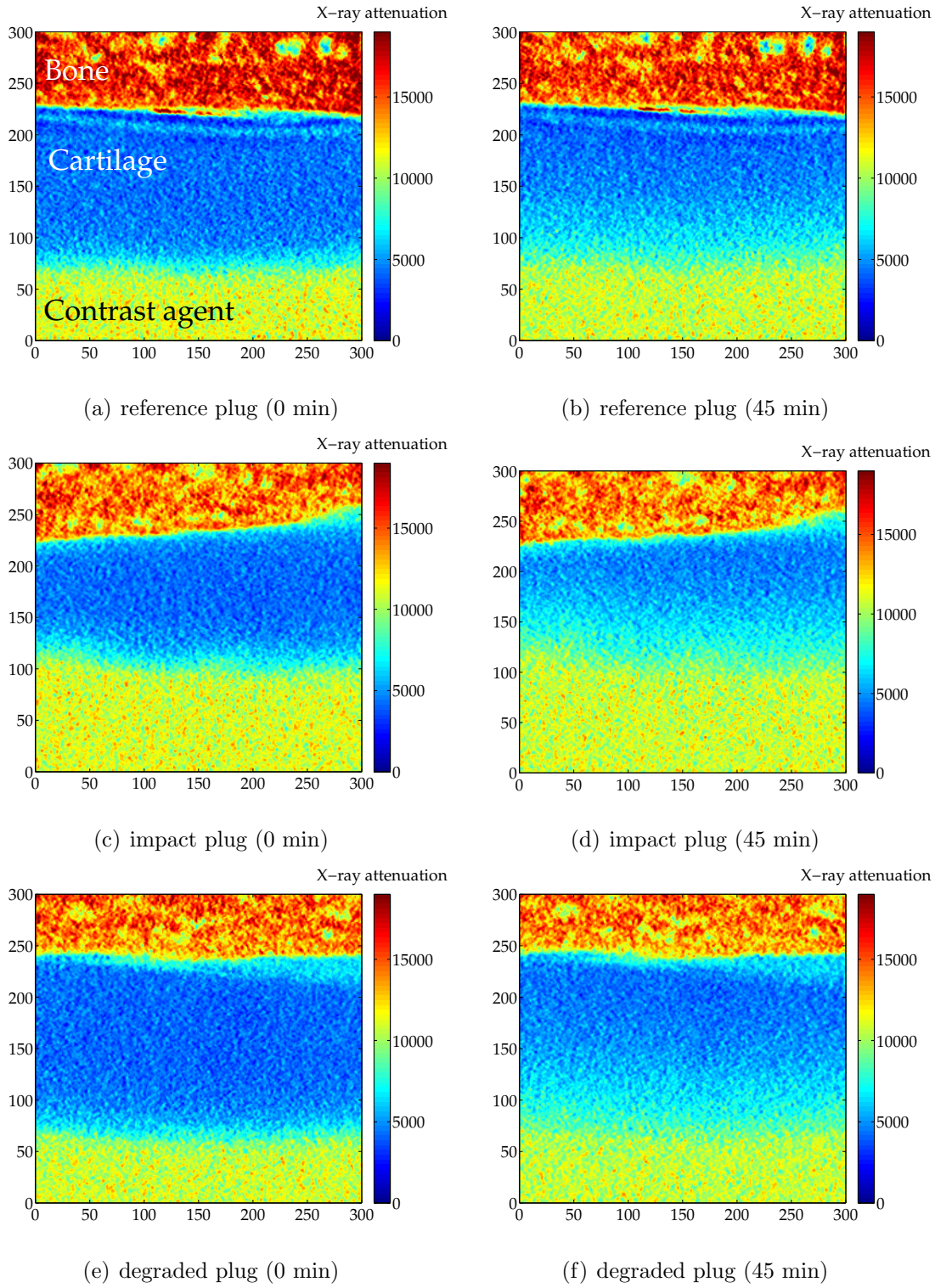

(a) reference plug (0 min)

(b) reference plug (45 min)

(c) impact plug (0 min)

(d) impact plug (45 min)

(e) degraded plug (0 min)

(f) degraded plug (45 min)

Figure 5.2: MicroCT images of the sample plugs using Hexabrix 15% solution. Images are averaged over 201 consecutive image slices. Hexabrix 15% solution allows the detection of cartilage injuries as elevated contrast agent concentration in the injured site. However, the evaluation of surface changes, such as crack, is challenging.

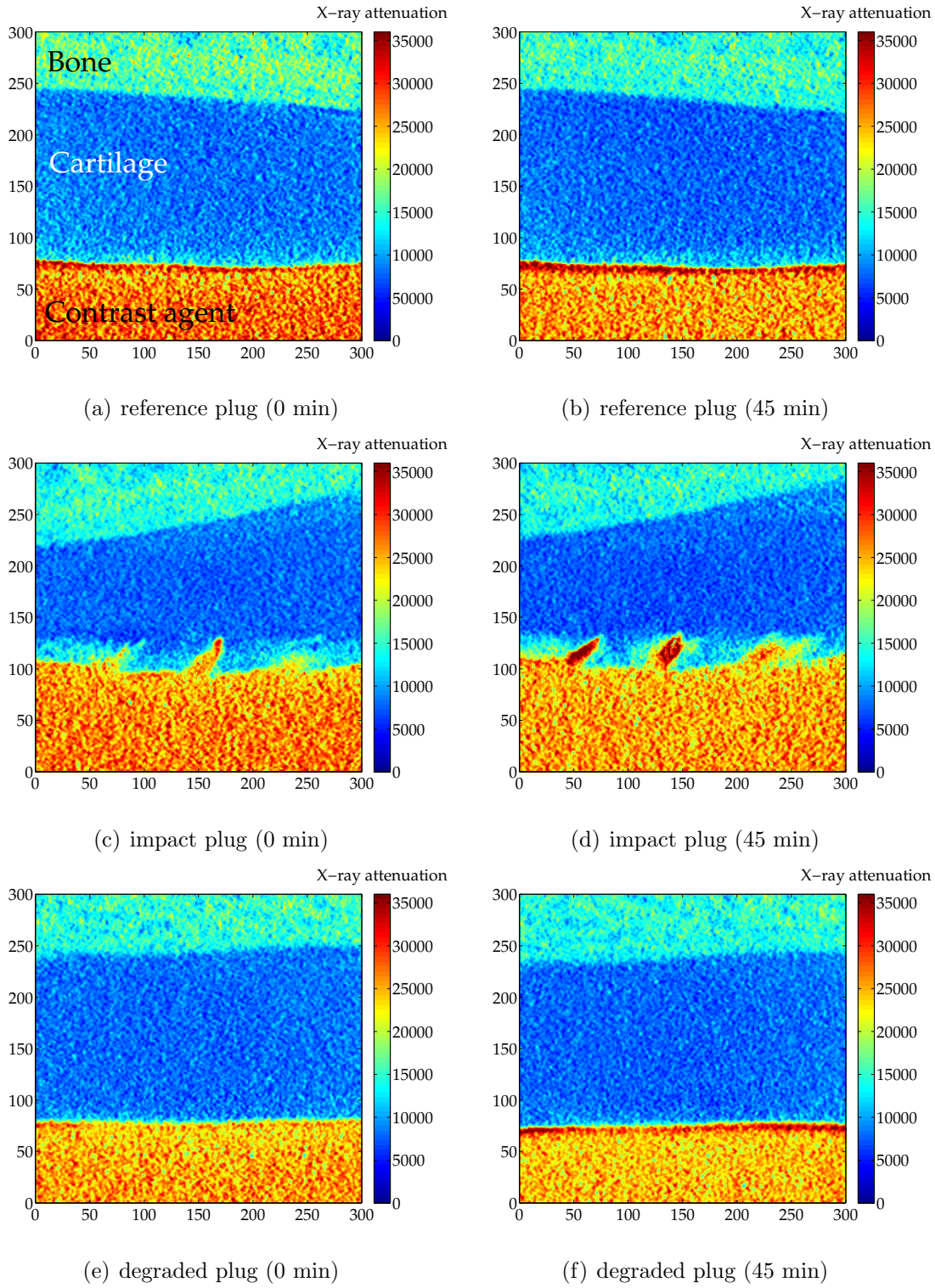

(a) reference plug (0 min)

(b) reference plug (45 min)

(c) impact plug (0 min)

(d) impact plug (45 min)

(e) degraded plug (0 min)

(f) degraded plug (45 min)

Figure 5.3: MicroCT images of the sample plugs using bismuth oxide nanoparticle suspension. Images are averaged over 201 consecutive image slices. BiNPs maintain the high contrast at the cartilage-contrast agent interface and allow the detection of cracks and other surface lesions. Nevertheless, diagnostics of subsurface injuries is infeasible.

of nanoparticles is large enough for keeping nanoparticles from diffusing into the cartilage despite the cartilage condition. Furthermore, the cracks and other surface unevenness can be detected easily from the microCT images of the impact plug with both 0-minute and 45-minute images (Fig. 5.3(c)-(d)). However, it is impossible to say anything about the condition of the cartilage under the surface i.e. internal lesions and loss of PGs. For example, there is no visible difference in reference plug and degraded plug even though it is known that the degraded plug suffers from severe loss of PGs and thus, the PG related changes in cartilage would get unnoticed.

Another interesting feature is that the bismuth oxide is agglomerating on the surface of the cartilage and especially to the cracks of the mechanically injured cartilage. This is most probably due to opposite charges of the cartilage and the nanoparticles. As previously mentioned, GAG molecules are negatively charged inducing an overall negative charge to the cartilage surface. On the contrary, the BiNPs have a high positive zeta potential implying high positive surface charge density. Thus, nanoparticles are drawn near the surface of the cartilage due to electric attraction. Since the sample plugs were imaged upside down, the gravity is irresponsible for the accumulation of the BiNP on the surface of the cartilage. This accumulation of the BiNPs on the surface of the cartilage would make the detection of superficial cartilage lesions, as well as the segmentation of the cartilage-contrast agent interface significantly easier as the contrast in articulating surface improves.

Since there is no knowledge about the secession of the positively charged nanoparticles attached to the cartilage surface *in vivo*, we decined the develop a improved dual contrast agent. For this reason, the BiNP surfaces were modified to change the surface charge density from postive to negative to prevent the nanoparticles from aggregating on the cartilage surface.

Since our dual contrast agent is a mixture of the Hexabrix 15% solution and the BiNP suspension, it should reflect all the good qualities observed with these two contrast agents. The dual contrast agent should allow the diagnostics of fresh cartilage injuries and degenerations conducting only one image 45 minutes after dual contrast agent administration. Thus, ioxaglate molecules should be able to diffuse into catilage freely, and nanoparticles should be able to maintain the high contrast at the cartilage-contrast agent interface. The microCT images at both time points using dual contrast agent for all three sample plugs are presented in the Fig. 5.4.

The lesions of the surface induced by the mechanical impact can be detected easily as the contrast at the cartilage-contrast agent interface remain remarkably distinct even 45 minutes after the immersion into dual contrast agent. However, as the contrast between the cartilage and surrounding contrast agent increases considerably, the visual evaluation of the contrast agent diffusion into the cartilage becomes more challenging. Thus, the more detailed evaluation of the contrast agent diffusion into

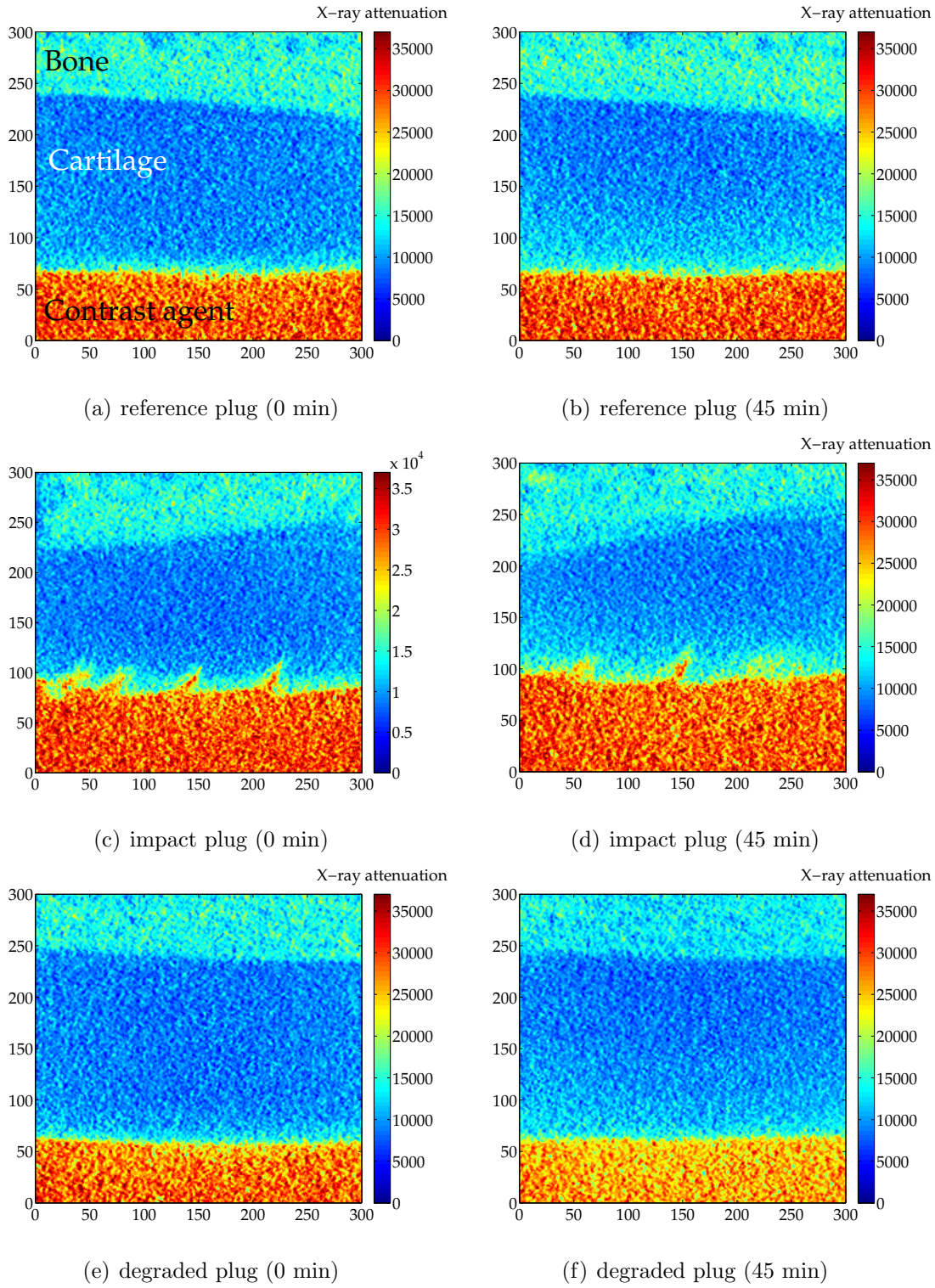

(a) reference plug (0 min)

(b) reference plug (45 min)

(c) impact plug (0 min)

(d) impact plug (45 min)

(e) degraded plug (0 min)

(f) degraded plug (45 min)

Figure 5.4: MicroCT images of the sample plugs using dual contrast agent. Images are averaged over 201 consecutive image slices. With the dual contrast agent the detection of superficial injuries is possible from the microCT images conducted 45 minutes after dual contrast agent immersion as we hyphotesized. However, based on these images, the evaluation of subsurface injuries is challenging.

cartilage have to be done by comparing the attenuation profiles.

5.2.2 The First Dual Contrast Agent - X-ray Attenuation Profiles

X-ray attenuation profiles are providing more detailed information about the condition of the cartilage. The attenuation profiles along the vertical direction of both damaged sample plugs in comparison with the reference plug immediately and 45 minutes after the immersion into the Hexabrix 15% solution are presented in Fig. 5.5. As can be seen, the X-ray attenuation profiles as the cartilage part are similar for every cartilage plug immediately after the sample plugs are immersed into Hexabrix 15% solution.

At 45 minutes after the immersion, the X-ray attenuation is higher in mechanically injured and enzymatically degraded cartilage. In both 45-minute images, the X-ray attenuation has increased more as compared to the reference plug. This implies that the diffusion of the contrast agent into cartilage is greater in both impact plug and degraded plug as compared to the reference plug. In a recent study by Kokkonen et al., histological analyses showed that mechanically injured tissue undergoes a minor PG loss [11]. Thus, the PG loss is at least partly responsible for the increased diffusion of the contrast agent into injured cartilage. Other reasons for greater contrast agent diffusion into mechanically injured cartilage may include additional structural and compositional changes e.g. in collagen and water content. These changes can increase the permeability of the cartilage and reduce the steric hindrance of collagen. The increased X-ray attenuation in damaged cartilage can be also visually observed from microCT images (Fig. 5.2). This perception has already been shown in previous studies [10] and [11]. Also for enzymatically degraded cartilage, the main reason for higher X-ray attenuation is the PG loss but also other structural and compositional changes that increase the contrast agent diffusion into degraded cartilage.

In Fig. 5.6 the attenuation profiles of the injured sample plugs are presented along the vertical direction in comparison with the reference plug immediately and 45 minutes after the immersion into the BiNP suspension where BiNPs were coated with TWEEN 80. Firstly, since the attenuation profile of the cartilage remains unchanged from the 0-minute to 45-minute attenuation profile we can state that the BiNPs are not diffusing into cartilage as hyphotesized. Thus, the nanoparticles maintain the distinctiveness of the interface between cartilage and surrounding contrast agent as hypothesized. These results were already observed from the microCT images (Fig. 5.3).

In addition, the gathering of the bismuth oxide on the surface of the cartilage and

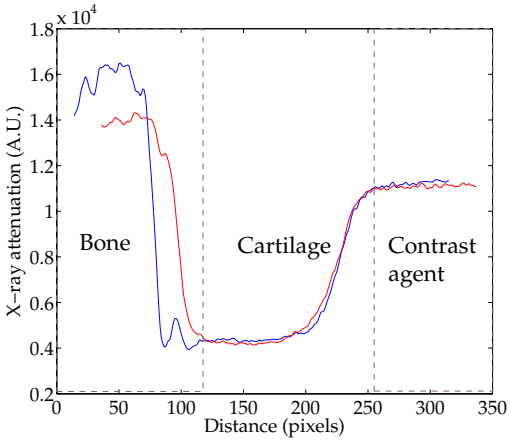

(a) reference plug as blue versus impact plug as red (0 min)

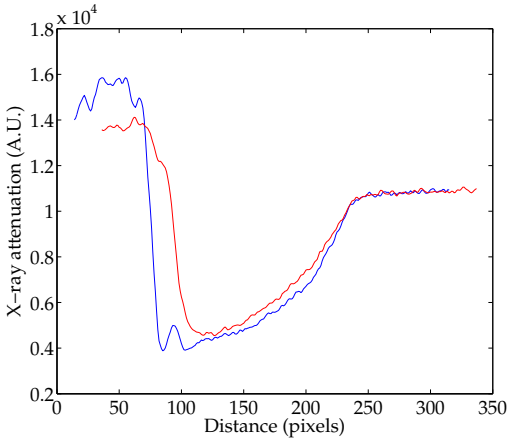

(b) reference plug versus impact plug (45 min)

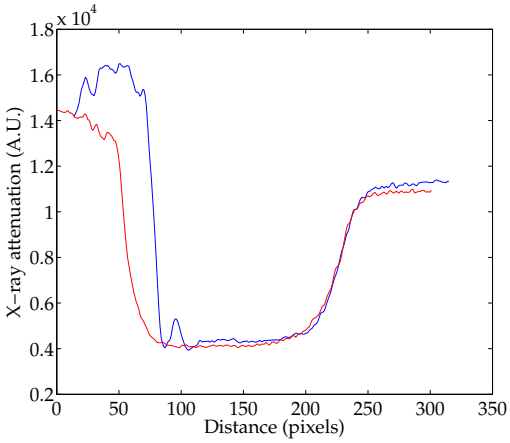

(c) reference plug versus degraded plug (0 min)

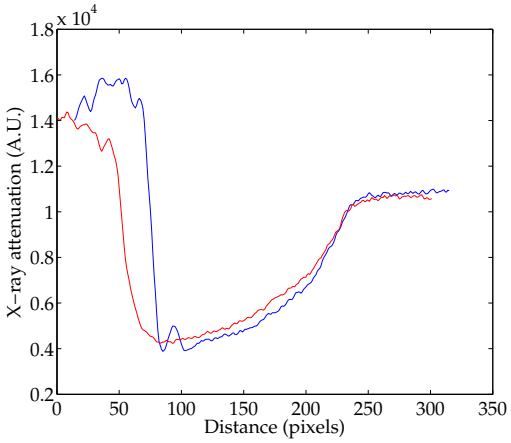

(d) reference plug versus degraded plug (45 min)

Figure 5.5: The attenuation profiles along the vertical direction using the Hexabrix 15% solution. The mechanically injured sample plug is compared with the reference plug (a) immediatelly after the contrast agent immersion and (b) 45 minutes after the immersion. The enzymatically degraded sample plug is compared with the reference plug (c) immediatelly after the contrast agent immersion and (d) 45 minutes after the immersion. The X-ray attenuation profiles of the reference plug are represented as blue and the X-ray attenuation profiles of the injured plugs are represented as red.

especially to the cracks of the mechanically injured cartilage can be seen also from the attenuation profiles as high peaks in Fig. 5.6. Owing to bismuth oxide gathering to the cracks of the mechanically injured sample plug, it is also easy to estimate the depth of the cracks caused by the impact with the BiNP suspension.

The X-ray attenuation profiles along the vertical direction of both injured sample plugs in comparison with the reference plug immediately and 45 minutes after the immersion into the dual contrast agent are presented in Fig. 5.7. In cartilage the attenuation profile should be similar to that imaged with Hexabrix 15% solution since the ioxagalte molecules should be able to move freely in the dual contrasta

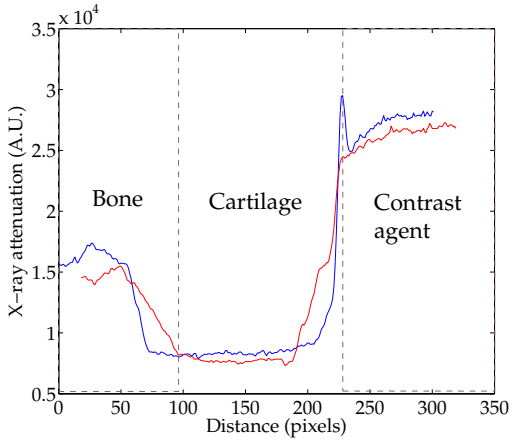

(a) reference plug as blue versus impact plug as red (0 min)

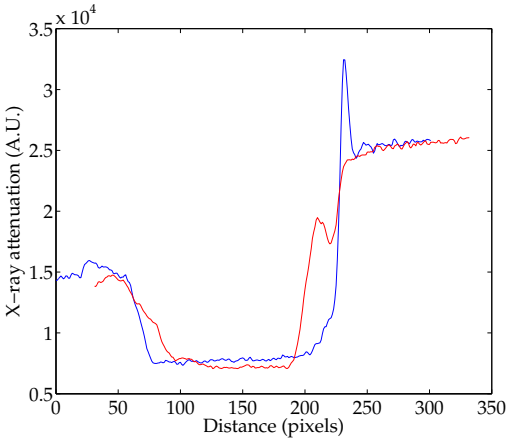

(b) reference plug versus impact plug (45 min)

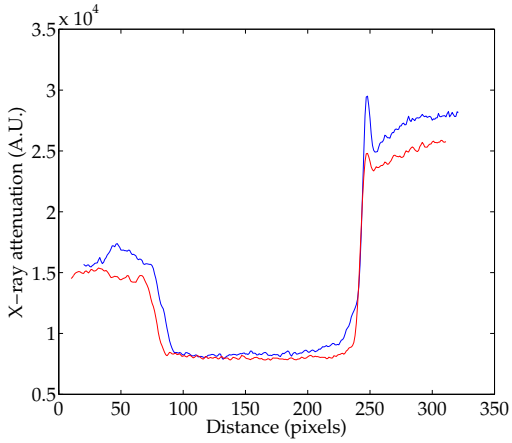

(c) reference plug versus degraded plug (0 min)

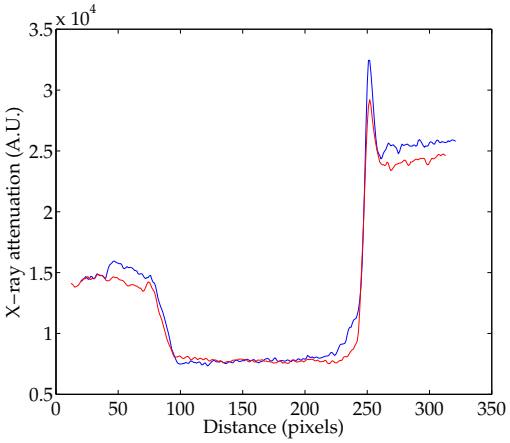

(d) reference plug versus degraded plug (45 min)

Figure 5.6: The attenuation profiles along the vertical direction using BiNP suspension. The mechanically injured sample plug is compared with the reference plug (a) immediatelly after the contrast agent immersion and (b) 45 minutes after the immersion. The enzymatically degraded sample plug is compared with the reference plug (c) immediatelly after the contrast agent immersion and (d) 45 minutes after the immersion. The X-ray attenuation profiles of the reference plug are represented as blue and the X-ray attenuation profiles of the injured plugs are represented as red.

agent similarly as in Hexabrix 15% solution. The X-ray attenuation profiles of the injured sample plug should be above the reference X-ray attenuation profile. Now, however, the ioxaglate in the dual contrast agent is unable to reach the same level of diffusion as in the Hexabrix 15% solution (Fig. 5.5 (d) vs. Fig. 5.7 (d)). Thus, we think that ioxaglate is not as free to diffuse into cartilage in dual contrast agent as in the Hexabrix 15% solution. This might be due to opposite charges of the ioxaglate molecules and BiNPs in the dual contrast agent causing the ioxaglate molecules and nanoparticles to agglomerate.

Another problem with this dual contrast agent is the especially high contrast

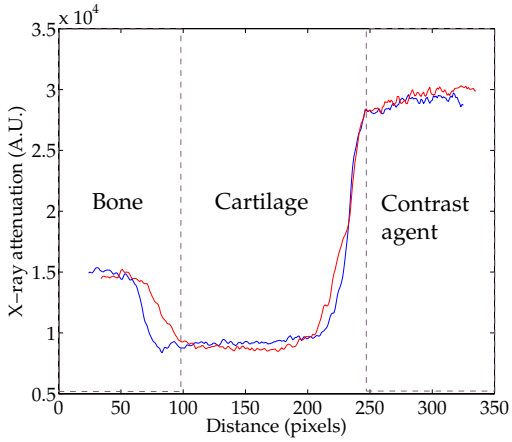

(a) reference plug as blue versus impact plug as red (0 min)

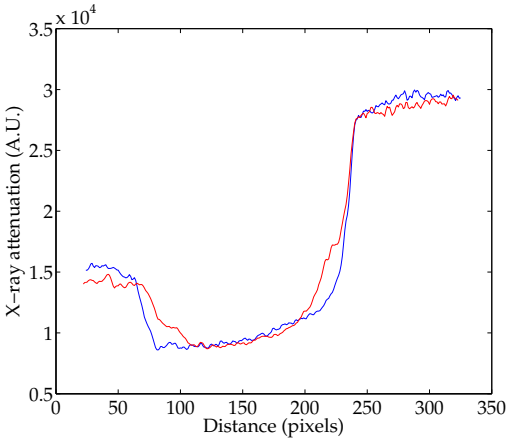

(b) reference plug versus impact plug (45 min)

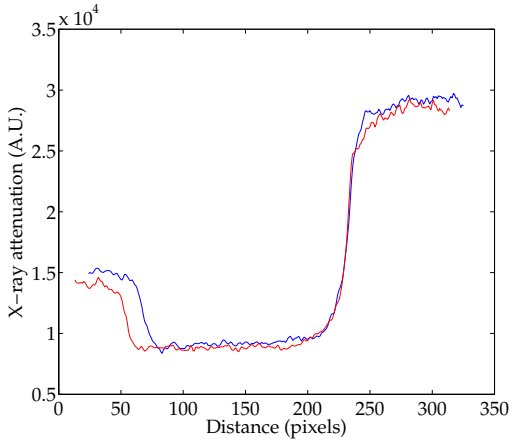

(c) reference plug versus degraded plug (0 min)

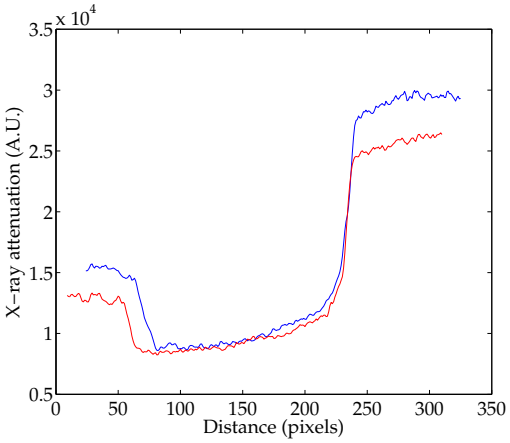

(d) reference plug versus degraded plug (45 min)

Figure 5.7: The attenuation profiles along the vertical direction using the dual contrast agent. The mechanically injured sample plug is compared with the reference plug (a) immediatelly after the contrast agent immersion and (b) 45 minutes after the immersion. The enzymatically degraded sample plug is compared with the reference plug (c) immediatelly after the contrast agent immersion and (d) 45 minutes after the immersion. The X-ray attenuation profiles of the reference plug are represented as blue and the X-ray attenuation profiles of the injured plugs are represented as red.

at the cartilage-contrast agent interface. This high contrast is unavailing for our purpose and thus signifying that the contrast could be decreased. This means that the concentration of the bismuth oxide could be decreased in the dual contrast agent decreasing also the concentration-dependent cytotoxicity of the dual contrast agent.

5.3 Improved Dual Contrast Agent

There are also a few factors that need to be solved before the dual contrast method can be implemented to more extensive studies. A major challenge in using nanoparticles in clinical use is their exposure for high salinity. High inorganic ion concen-

tration can affect the stability of the suspension. Inorganic ions can interact with charged surfaces of the nanoparticles, thus changing the zeta potential of the particle suspension. In the worst case, inorganic ion adsorption can even lead to charge reversal of the surface decreasing the repulsive forces of the nanoparticles. Thus, adjusting the osmolarity of the suspension to the physiological osmolarity with NaCl is probably disturbing the stability of the suspension as well as causing aggregation of the nanoparticles at some level. Aggregation occurs whenever the Brownian motion and the attractive forces of the particles are greater than the repulsive forces [112].

Secondly, the stability of the suspension could be improved further. First, the stability improves as the concentration of the nanoparticle suspension decreases. Thus, another reason behind the decision to decrease the concentration of bismuth oxide for the improved dual contrast agent was to achieve more stable nanoparticle suspension. Second, the stability of the suspension can be improved by choosing a different coating polymer. According to our preliminary tests with different coating polymer, PEG turned out to produce the most stable suspension and thus for the improved dual contrast agent TWEEN 80 was replaced by PEG. The nanoparticles in TWEEN 80 suspension were observed to settle down in a shorter time as the sample tubes containing both suspensions were kept on the table stationary during the monitoring. The consistency of the resulting suspension was also another advantage of PEG over TWEEN 80. Usage of TWEEN 80 changed the consistency of the BiNP suspension more into foam-like which made the suspension containing TWEEN 80 challenging to apply for CECT imaging.

Thirdly, the charge of the nanoparticles could be changed to keep nanoparticles and ioxaglate molecules from adhering together due to electrostatic forces by the surface modification. In the first batch of BiNP solution, the nanoparticles were charged positively as the ioxaglate molecules had negative charge. By changing the charge of the nanoparticles to negative, a strong repulsion between nanoparticles and ioxaglate molecules can be generated in the dual contrast agents. To prevent aggregation, the surface of the nanoparticles was modified to have negative charge density using citric acid. The zeta potential distribution of the PEG-coated BiNP suspension and the surface modified BiNP suspension is shown in Fig. 5.8. Zeta potential was measured to be 59.1 for PEG-coated and -38.3 mV surface modified BiNP suspension which implied that the stability of both suspensions is good. Zeta potential of the surface modified BiNP suspension also implies that the nanoparticles have negative surface charge density close to measured zeta potential since the zeta potential measurement was conducted in distilled water at neutral pH.

With the first dual contrast agent, in which the BiNPs were coated with TWEEN 80, we observed that the ioxaglate penetration into cartilage in dual contrast agent was not corresponding the ioxaglate penetration in Hexabrix 15% solution. Thus

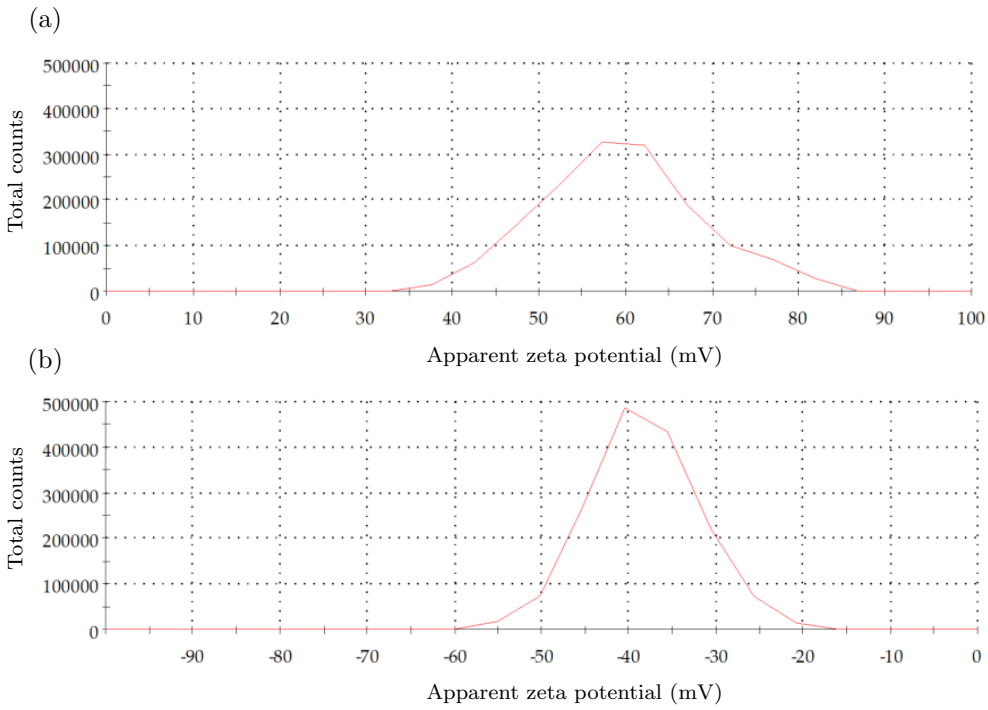

Figure 5.8: (a) Zeta potential distribution of BiNP suspension with PEG coating polymer. Zeta potential was measured to be 59.1 ± 9.1 mV. (b) Zeta potential of the surface modified BiNP suspension. Zeta potential was measured to be -38.3 ± 6.28 mV.

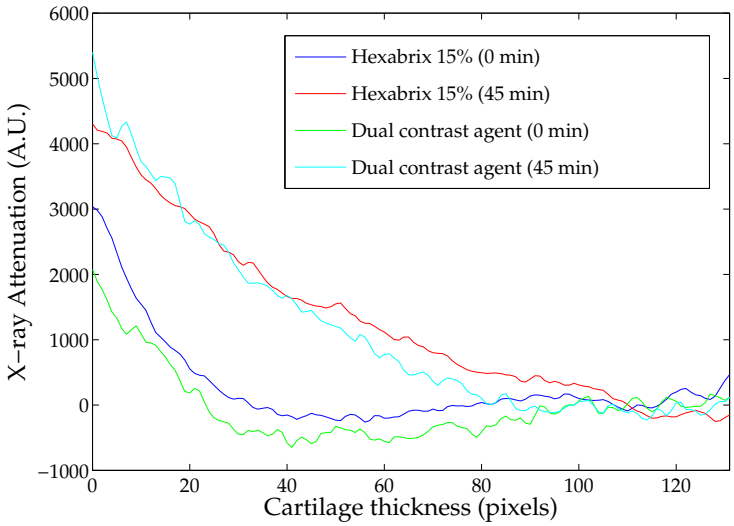

Figure 5.9: The X-ray Attenuation profiles of cartilage at both time points with the improved dual contrast agent and Hexabrix 15% solution. The average X-ray attenuation value of cartilage before the contrast agent immersion (i.e. baseline) was subtracted from that after the immersion. In this way, only the attenuation profile of the ioxaglate in the cartilage is achieved. The surface of the articulatingcartilage is on the left and the cartilage-bone intreface on the right.

as a first test with the improved dual contrast agent, we compared the ioxaglate penetrations with Hexabrix 15% solution using a degraded osteochondral plug. The results of this preliminary test are presented in Fig. 5.9. Now, the attenuation profiles show that the penetration of ioxaglate in improved dual contrast agent corresponds the ioxaglate penetration observed with the Hexabrix 15% solution. Thus, the dual contrast agent seems to have over come the challenges observed during the preparation of the first dual contrasts agent and is hence ready for more extensive studies.

6. CONCLUSIONS

In this thesis, the potential and feasibility of the dual contrast method for CECT diagnostics of cartilage injuries *in vitro* was developed and introduced for the first time. Using the current methods, articular cartilage lesions are diagnosed conducting CECT images immediately after and at 45 minutes after contrast agent injection into the synovial fluid. The first image is required for accurate segmentation of the cartilage surface since the contrast between the cartilage and synovial fluid deteriorates due to contrast agent diffusion into cartilage. Delayed imaging, at 45 minutes after the administration, allows the detection of cartilage injuries as elevated contrast agent concentration at injured or degenerated tissue. However, according to our hypothesis, the dual contrast method would enable simultaneous imaging of cartilage lesions and segmentation of the cartilage-contrast agent interface from image conducted 45 minutes after the contrast agent administration into the synovial fluid. Thus as an outcome, the dual contrast method would enhance the diagnostics of fresh cartilage injuries and enable better planning of repair operations.

The feasibility of the dual contrast method was evaluated by imaging osteochondral plugs in three different contrast agents (Hexabrix 15% solution, BiNP suspension, and dual contrast agent) using a microCT device. Two of the plugs were injured; one mechanically and other enzymatically. The remaining osteochondral plug served as a reference. The dual contrast agent, developed in this study, is a mixture of an iodine-based contrast agent ioxaglate (Hexabrix) and a suspension of nano-sized bismuth oxide particles. The large size of the nanoparticles prevents them from diffusing into cartilage; hence, the contrast at the synovial fluid-cartilage interface can be retained at a high level due to the nanoparticles, even at the 45 minutes after the contrast agent administration. Conversely, the diffusion of the ioxaglate into cartilage allows the quantitative evaluation of the cartilage composition. As a result, the condition of the cartilage can be evaluated conducting only one image after 45 minutes from the contrast agent administration.

At the beginning, the first version of the dual contrast agent was tested. This dual contrast agent, however, was unable to meet the requirements that we had for the nanoparticle suspension. First of all, the stability of the contrast agent was poor. Secondly, the positive surface charge caused the nanoparticles to agglomerate with the ioxaglate molecules in the dual contrast agent. For these reasons, we prepared

another improved dual contrast agent containing PEG as a coating polymer and modified the surface charge density of the nanoparticles from positive to negative to avoid too strong interactions between the nanoparticle and cartilage tissue which may be harmful *in vivo*.

The improved dual contract agent was tested with an enzymatically degraded osteochondral plug. Obtained results were promising since this time the ioxaglate molecules were able to diffuse into cartilage similarly as in the situation where only Hexabrix 15% solution was used as a contrast agent. This implies that with the improved dual contrast agent, the condition of the cartilage can be evaluated as we hypothesised. However, further research needs to be conducted to verify the feasibility of the dual contrast method.

As a long-term goal, we are aiming to introduce the dual contrast method for the clinical use. However in the clinical use, two factors will slightly decrease the sensitivity of the dual contrast method. Firstly, the contrasts agents are diluted into synovial fluid reducing the concentration of the ioxaglate and BiNP in the final solution. Secondly, the efflux of the contrast agent from the joint capsule after the contrasts agent administration into synovial fluid will also slightly reduce the concentration. Furthermore, the resolution of clinical CT devices is lower (usually >200 μm) making, for example, the detection of cartilage surface changes more challenging. The difficulty of detecting cracks and other surface changes with lower resolution is mainly due to partial volume effect as well as decreases number of pixels representing a crack in the cartilage surface. To examine the applicability of the dual contrast method in clinical use more profoundly, the method will also be tested in cadaveric human knee *in situ* as well as in equine joints *in vivo* later in the future.

To conclude, the dual contrast method seems to be a useful tool for the fresh cartilage injury diagnostics but the method can be still improved further. The next step in this project is to conduct more extensive microCT measurements with ten new patellae to study the feasibility of dual contrast method for more detailed cartilage injury diagnostics in a long way to final product to be utilized in clinical use.

BIBLIOGRAPHY

[1] **Borrelli Jr, J., Zhu, Y., Burns, M., Sandell, L., and Silva, M.J.**, Cartilage tolerates single impact loads of as much as half the joint fracture threshold. *Clinical Orthopaedics and Related Research*, 426: 266–273. 2004.

[2] **Brown, T.D., Johnston, R.C., Saltzman, C.L., Marsh, J.L., and Buckwalter, J.A.**, Posttraumatic osteoarthritis: a first estimate of incidence, prevalence, and burden of disease. *Journal of Orthopaedic Trauma*, 20(10): 739–744. 2006.

[3] **Blevins, F.T., Rodrigo, J.J., and Silliman, J.**, Treatment of articular cartilage defects in athletes: an analysis of functional outcome and lesion appearance. *Orthopedics*, 21(7): 761. 1998.

[4] **Anderson, D.D., Chubinskaya, S., Guilak, F., Martin, J.A., Oegema, T.R., Olson, S.A., and Buckwalter, J.A.**, Post-traumatic osteoarthritis: Improved understanding and opportunities for early intervention. *Journal of Orthopaedic Research*, 29(6): 802–809. 2011.

[5] **Olson, S.A., Furman, B.D., Kraus, V.B., Huebner, J.L., and Guilak, F.**, Therapeutic Opportunities to Prevent Post-Traumatic Arthritis: Lessons from the Natural History of Arthritis after Articular Fracture. *Journal of Orthopaedic Research*. 2015.

[6] **Buckwalter, J. and Mankin, H.**, Articular cartilage: Part II. *Journal of bone and joint surgery*, 79(4): 612. 1997.

[7] **Buckwalter, J.A. and Martin, J.**, Degenerative joint disease. In *Clinical symposia (Summit, NJ: 1957)*, volume 47, p. 1. 1995.

[8] **Silvast, T., Jurvelin, J., Lammi, M., and Töyräs, J.**, pQCT study on diffusion and equilibrium distribution of iodinated anionic contrast agent in human articular cartilage–associations to matrix composition and integrity. *Osteoarthritis and Cartilage*, 17(1): 26–32. 2009.

[9] **Silvast, T., Jurvelin, J., Aula, A., Lammi, M., and Töyräs, J.**, Contrast agent-enhanced computed tomography of articular cartilage: association with tissue composition and properties. *Acta Radiologica*, 50(1): 78–85. 2009.

[10] **Kokkonen, H.T., Aula, A.S., Kröger, H., Suomalainen, J.S., Lammentausta, E., Mervaala, E., Jurvelin, J.S., and Töyräs, J.**, Delayed computed tomography arthrography of human knee cartilage in vivo. *Cartilage*, 3(4): 334–341. 2012.

[11] **Kokkonen, H., Jurvelin, J., Tiitu, V., and Töyräs, J.**, Detection of mechanical injury of articular cartilage using contrast enhanced computed tomography. *Osteoarthritis and Cartilage*, 19(3): 295–301. 2011.

[12] **Kalender, W.A.**, *Computed tomography: fundamentals, system technology, image quality, applications*. John Wiley & Sons. 2011.

[13] **Briand, G.G. and Burford, N.**, Bismuth compounds and preparations with biological or medicinal relevance. *Chemical Reviews*, 99(9): 2601–2658. 1999.

[14] **Mow, V.C., Ratcliffe, A., and Poole, A.R.**, Cartilage and diarthrodial joints as paradigms for hierarchical materials and structures. *Biomaterials*, 13(2): 67–97. 1992.

[15] **Buckwalter, J., Rosenberg, L., and Hunziker, E.**, Articular cartilage: composition, structure, response to injury, and methods of facilitating repair. *Articular Cartilage and Knee Joint Function: Basic Science and Arthroscopy. J. Ewing, editor^ editors. Raven Press ltd., New York*, pp. 19–56. 1990.

[16] **Fox, A.J.S., Bedi, A., and Rodeo, S.A.**, The basic science of articular cartilage: structure, composition, and function. *Sports Health: A Multidisciplinary Approach*, 1(6): 461–468. 2009.

[17] **Stockwell, R.**, The interrelationship of cell density and cartilage thickness in mammalian articular cartilage. *Journal of Anatomy*, 109(Pt 3): 411. 1971.

[18] **Mow, V., Fithian, D., and Kelly, M.**, Fundamentals of articular cartilage and meniscus biomechanics. *Articular Cartilage and Knee Joint Function: Basic Science and Arthroscopy*, pp. 1–18. 1990.

[19] **Buckwalter, J. and Mankin, H.**, Articular cartilage: tissue design and chondrocyte-matrix interactions. *Instructional Course Lectures*, 47: 477–486. 1997.

[20] **Xia, Y., Moody, J., Alhadlaq, H., Burton-Wurster, N., and Lust, G.**, Characteristics of topographical heterogeneity of articular cartilage over the joint surface of a humeral head. *Osteoarthritis and Cartilage*, 10(5): 370–380. 2002.

[21] **Bank, R., Bayliss, M., Lafeber, F., Maroudas, A., and Tekoppele, J.**, Ageing and zonal variation in post-translational modification of collagen in normal human articular cartilage. *Biochemical Journal*, 330: 345–351. 1998.

[22] **Eyre, D.**, Collagen of articular cartilage. *Arthritis Research*, 4(1): 30–35. 2002.

[23] **Huber, M., Trattnig, S., and Lintner, F.**, Anatomy, biochemistry, and physiology of articular cartilage. *Investigative Radiology*, 35(10): 573–580. 2000.

[24] **Venn, M. and Maroudas, A.**, Chemical composition and swelling of normal and osteoarthrotic femoral head cartilage. I. Chemical composition. *Annals of the Rheumatic Diseases*, 36(2): 121–129. 1977.

[25] **Buckwalter, J.A.**, Articular cartilage: injuries and potential for healing. *Journal of Orthopaedic & Sports Physical Therapy*, 28(4): 192–202. 1998.

[26] **Maroudas, A.**, Physicochemical properties of cartilage in the light of ion exchange theory. *Biophysical Journal*, 8(5): 575. 1968.

[27] **JONES, I.L., LARSSON, S.E., and LEMPERG, R.**, The glycosaminoglycans of human articular cartilage: concentration and distribution in different layers in the adult individual. *Clinical Orthopaedics and Related Research*, 127: 257–264. 1977.

[28] **Lane Smith, R., Trindade, M., Ikenoue, T., Mohtai, M., Das, P., Carter, D., Goodman, S., and Schurman, D.**, Effects of shear stress on articular chondrocyte metabolism. *Biorheology*, 37(1-2): 95–107. 2000.

[29] **Huber, M., Trattnig, S., and Lintner, F.**, Anatomy, biochemistry, and physiology of articular cartilage. *Investigative Radiology*, 35(10): 573–580. 2000.

[30] **Martin, J.A. and Buckwalter, J.A.**, The role of chondrocyte senescence in the pathogenesis of osteoarthritis and in limiting cartilage repair. *The Journal of Bone & Joint Surgery*, 85(suppl 2): 106–110. 2003.

[31] **Jay, G., Torres, J., Warman, M., Laderer, M., and Breuer, K.**, The role of lubricin in the mechanical behavior of synovial fluid. *Proceedings of the National Academy of Sciences*, 104(15): 6194–6199. 2007.

[32] **Ateshian, G.A.**, The role of interstitial fluid pressurization in articular cartilage lubrication. *Journal of Biomechanics*, 42(9): 1163–1176. 2009.

[33] **Buckwalter, J.**, Articular cartilage injuries. *Clinical Orthopaedics and Related Research*, 402: 21–37. 2002.

[34] **Buckwalter, J.A.**, Mechanical injuries of articular cartilage. *The Iowa Orthopaedic Journal*, 12: 50. 1992.

[35] **Borrelli Jr, J., Zhu, Y., Burns, M., Sandell, L., and Silva, M.J.**, Cartilage tolerates single impact loads of as much as half the joint fracture threshold. *Clinical Orthopaedics and Related Research*, 426: 266–273. 2004.

[36] **Brown, T.D., Johnston, R.C., Saltzman, C.L., Marsh, J.L., and Buckwalter, J.A.**, Posttraumatic osteoarthritis: a first estimate of incidence, prevalence, and burden of disease. *Journal of Orthopaedic Trauma*, 20(10): 739–744. 2006.

[37] **Kokkonen, H.T., Suomalainen, J.S., Joukainen, A., Kröger, H., Sirola, J., Jurvelin, J.S., Salo, J., and Töyräs, J.**, In vivo diagnostics of human knee cartilage lesions using delayed CBCT arthrography. *Journal of Orthopaedic Research*, 32(3): 403–412. 2014.

[38] **Carney, S.L., Billingham, M.E., Muir, H., and Sandy, J.D.**, Demonstration of increased proteoglycan turnover in cartilage explants from dogs with experimental osteoarthritis. *Journal of Orthopaedic Research*, 2(3): 201–206. 1984.

[39] **Lin, P.M., Chen, C.T.C., and Torzilli, P.A.**, Increased stromelysin-1 (MMP-3), proteoglycan degradation (3B3-and 7D4) and collagen damage in cyclically load-injured articular cartilage. *Osteoarthritis and Cartilage*, 12(6): 485–496. 2004.

[40] **Buckwalter, J.A.**, Mechanical injuries of articular cartilage. *The Iowa Orthopaedic Journal*, 12: 50. 1992.

[41] **Silvast, T., Jurvelin, J., Lammi, M., and Töyräs, J.**, pQCT study on diffusion and equilibrium distribution of iodinated anionic contrast agent in human articular cartilage–associations to matrix composition and integrity. *Osteoarthritis and Cartilage*, 17(1): 26–32. 2009.

[42] **Silvast, T., Jurvelin, J., Aula, A., Lammi, M., and Töyräs, J.**, Contrast agent-enhanced computed tomography of articular cartilage: association with tissue composition and properties. *Acta Radiologica*, 50(1): 78–85. 2009.

[43] **Dirschl, D.R., Marsh, J.L., Buckwalter, J.A., Gelberman, R., Olson, S.A., Brown, T.D., and Llinias, A.**, Articular fractures. *Journal of the American Academy of Orthopaedic Surgeons*, 12(6): 416–423. 2004.

[44] **Pridie, K. and Gordon, G.**, A method of resurfacing osteoarthritic knee joints. In *Journal of Bone and Joint Surgery-British Volume*, volume 41, pp. 618–619. 1959.

[45] **Brittberg, M., Lindahl, A., Nilsson, A., Ohlsson, C., Isaksson, O., and Peterson, L.**, Treatment of deep cartilage defects in the knee with autologous chondrocyte transplantation. *New England Journal of Medicine*, 331(14): 889–895. 1994.

[46] **Hangody, L. and Füles, P.**, Autologous osteochondral mosaicplasty for the treatment of full-thickness defects of weight-bearing joints. *The Journal of Bone & Joint Surgery*, 85(suppl 2): 25–32. 2003.

[47] **Webb, W.R., Brant, W.E., and Major, N.M.**, *Fundamentals of body CT*. Elsevier Health Sciences. 2006.

[48] **Buzug, T.M.**, *Computed tomography: from photon statistics to modern cone-beam CT*. Springer Science & Business Media. 2008.

[49] **Michael, G.**, X-ray computed tomography. *Physics Education*, 36(6): 442. 2001.

[50] **Kalender, W.A.**, X-ray computed tomography. *Physics in Medicine and Biology*, 51(13): R29. 2006.

[51] **Romans, L.E.**, *"Contrast agent" in Computed tomography for technologists: Exam review*. Lippincott Williams & Wilkins. 2010.

[52] **Attwood, D.**, *Soft X-rays and extreme ultraviolet radiation*. Cambridge University. 1999, 2 pp.

[53] **Heggie, J.C.**, *Applied imaging technology*. Ph.D. thesis, School of Medical Sciences, RMIT University, Melbourne. 2001.

[54] **McKetty, M.H.**, The AAPM/RSNA physics tutorial for residents. X-ray attenuation. *RadioGraphics*, 18(1): 151–163. 1998.

[55] **Macovski, A.**, *Medical imaging systems*. Prentice-Hall, New Jersey. 1983.

[56] **Zeng, G.**, Image reconstruction – a tutorial. *Computerized Medical Imaging and Graphics*, 25(2): 97–103. 2001.

[57] **Boas, F.E. and Fleischmann, D.**, CT artifacts: causes and reduction techniques. *Imaging in Medicine*, 4(2): 229–240. 2012.

[58] **Zhang, Y., Zhang, L., Zhu, X.R., Lee, A.K., Chambers, M., and Dong, L.**, Reducing metal artifacts in cone-beam CT images by preprocessing projection data. *International Journal of Radiation Oncology* Biology* Physics*, 67(3): 924–932. 2007.

[59] **Barrett, J.F. and Keat, N.**, Artifacts in CT: recognition and avoidance 1. *Radiographics*, 24(6): 1679–1691. 2004.

[60] **Flohr, T.G., Schaller, S., Stierstorfer, K., Bruder, H., Ohnesorge, B.M., and Schoepf, U.J.**, Multi–Detector Row CT Systems and Image-Reconstruction Techniques 1. *Radiology*, 235(3): 756–773. 2005.

[61] **Hsieh, J.**, Computed tomography: principles, design, artifacts, and recent advances. SPIE Bellingham, WA. 2009.

[62] **Scarfe, W.C. and Farman, A.G.**, What is cone-beam CT and how does it work? *Dental Clinics of North America*, 52(4): 707–730. 2008.

[63] **Roberts, J., Drage, N., Davies, J., and Thomas, D.W.**, Effective dose from cone beam CT examinations in dentistry. *The British Journal of Radiology*. 2014.

[64] **Loubele, M., Maes, F., Jacobs, R., van Steenberghe, D., White, S., and Suetens, P.**, Comparative study of image quality for MSCT and CBCT scanners for dentomaxillofacial radiology applications. *Radiation Protection Dosimetry*, 129(1-3): 222–226. 2008.

[65] **Suomalainen, A., Kiljunen, T., Käser, Y., Peltola, J., and Kortesniemi, M.**, Dosimetry and image quality of four dental cone beam computed tomography scanners compared with multislice computed tomography scanners. *Dentomaxillofacial Radiology*. 2014.

[66] **Scarfe, W.C., Farman, A.G., Sukovic, P., et al.**, Clinical applications of cone-beam computed tomography in dental practice. *Journal-Canadian Dental Association*, 72(1): 75. 2006.

[67] **Sandborg, M.**, Computed Tomography: Physical principles and biohazards. 1995.

[68] **Smith-Bindman, R., Lipson, J., Marcus, R., Kim, K.P., Mahesh, M., Gould, R., de González, A.B., and Miglioretti, D.L.**, Radiation dose associated with common computed tomography examinations and the associated lifetime attributable risk of cancer. *Archives of Internal Medicine*, 169(22): 2078–2086. 2009.

[69] **de González, A.B., Mahesh, M., Kim, K.P., Bhargavan, M., Lewis, R., Mettler, F., and Land, C.**, Projected cancer risks from computed tomographic scans performed in the United States in 2007. *Archives of Internal Medicine*, 169(22): 2071–2077. 2009.

[70] **Goldman, L.W.**, Principles of CT: radiation dose and image quality. *Journal of Nuclear Medicine Technology*, 35(4): 213–225. 2007.

[71] **Goldman, L.W.**, Principles of CT: multislice CT. *Journal of Nuclear Medicine Technology*, 36(2): 57–68. 2008.

[72] **Yu, S.B. and Watson, A.D.**, Metal-based X-ray contrast media. *Chemical Reviews*, 99(9): 2353–2378. 1999.

[73] **Lusic, H. and Grinstaff, M.W.**, X-ray-computed tomography contrast agents. *Chemical Reviews*, 113(3): 1641–1666. 2012.

[74] **McClennan, B.L.**, Preston M. Hickey memorial lecture. Ionic and nonionic iodinated contrast media: evolution and strategies for use. *AJR. American Journal of Roentgenology*, 155(2): 225–233. 1990.

[75] **Singh, J. and Daftary, A.**, Iodinated contrast media and their adverse reactions. *Journal of Nuclear Medicine Technology*, 36(2): 69–74. 2008.

[76] **Lee, N., Choi, S.H., and Hyeon, T.**, Nano-Sized CT Contrast Agents. *Advanced Materials*, 25(19): 2641–2660. 2013.

[77] **Cole, L.E., Ross, R.D., Tilley, J.M., Vargo-Gogola, T., and Roeder, R.K.**, Gold nanoparticles as contrast agents in x-ray imaging and computed tomography. *Nanomedicine*, 10(2): 321–341. 2015.

[78] **Pietsch, H.**, CT contrast agents. In *Small Animal Imaging*, pp. 141–149, Springer. 2011.

[79] **Min, Y., Akbulut, M., Kristiansen, K., Golan, Y., and Israelachvili, J.**, The role of interparticle and external forces in nanoparticle assembly. *Nature Materials*, 7(7): 527–538. 2008.

[80] **Kango, S., Kalia, S., Celli, A., Njuguna, J., Habibi, Y., and Kumar, R.**, Surface modification of inorganic nanoparticles for development of organic–inorganic nanocomposites – A review. *Progress in Polymer Science*, 38(8): 1232–1261. 2013.

[81] **Alqathami, M., Blencowe, A., Yeo, U., Franich, R., Doran, S., Qiao, G., and Geso, M.**, Enhancement of radiation effects by bismuth oxide nanoparticles for kilovoltage x-ray beams: a dosimetric study using a novel multi-compartment 3D radiochromic dosimeter. In *Journal of Physics: Conference Series*, volume 444, p. 012025, IOP Publishing. 2013.

[82] **Willmann, J.K., van Bruggen, N., Dinkelborg, L.M., and Gambhir, S.S.**, Molecular imaging in drug development. *Nature Reviews Drug Discovery*, 7(7): 591–607. 2008.

[83] **Lanza, G.M., Winter, P., Caruthers, S., Schmeider, A., Crowder, K., Morawski, A., Zhang, H., Scott, M.J., and Wickline, S.A.**, Novel paramagnetic contrast agents for molecular imaging and targeted drug delivery. *Current Pharmaceutical Biotechnology*, 5(6): 495–507. 2004.

[84] **Erathodiyil, N. and Ying, J.Y.**, Functionalization of inorganic nanoparticles for bioimaging applications. *Accounts of Chemical Research*, 44(10): 925–935. 2011.

[85] **Shilo, M., Reuveni, T., Motiei, M., and Popovtzer, R.**, Nanoparticles as computed tomography contrast agents: current status and future perspectives. *Nanomedicine*, 7(2): 257–269. 2012.

[86] **Nelson, P.**, *Biological physics*. WH Freeman New York. 2003.

[87] **Cussler, E.L.**, *Diffusion: mass transfer in fluid systems*. Cambridge University Press. 2009.

[88] **Donnan, F.G.**, The theory of membrane equilibria. *Chemical Reviews*, 1(1): 73–90. 1924.

[89] **Gray, M.L., Burstein, D., Kim, Y.J., and Maroudas, A.**, Magnetic resonance imaging of cartilage glycosaminoglycan: basic principles, imaging technique, and clinical applications. *Journal of Orthopaedic Research*, 26(3): 281–291. 2008.

[90] **Maroudas, A.**, Physicochemical properties of cartilage in the light of ion exchange theory. *Biophysical Journal*, 8(5): 575. 1968.

[91] **Bashir, A., Gray, M.L., and Burstein, D.**, Gd-DTPA2- as a measure of cartilage degradation. *Magnetic Resonance in Medicine*, 36(5): 665–673. 1996.

[92] **Salo, E.N., Nissi, M., Kulmala, K., Tiitu, V., Töyräs, J., and Nieminen, M.**, Diffusion of Gd-DTPA 2- into articular cartilage. *Osteoarthritis and Cartilage*, 20(2): 117–126. 2012.

[93] **Kallioniemi, A., Jurvelin, J., Nieminen, M., Lammi, M., and Töyräs, J.**, Contrast agent enhanced pQCT of articular cartilage. *Physics in Medicine and Biology*, 52(4): 1209. 2007.

[94] **Torzilli, P.A., Arduino, J.M., Gregory, J.D., and Bansal, M.**, Effect of proteoglycan removal on solute mobility in articular cartilage. *Journal of Biomechanics*, 30(9): 895–902. 1997.

[95] **Nimer, E., Schneiderman, R., and Maroudas, A.**, Diffusion and partition of solutes in cartilage under static load. *Biophysical Chemistry*, 106(2): 125–146. 2003.

[96] **Silvast, T.S., Kokkonen, H.T., Jurvelin, J.S., Quinn, T.M., Nieminen, M.T., and Töyräs, J.**, Diffusion and near-equilibrium distribution of MRI and CT contrast agents in articular cartilage. *Physics in Medicine and Biology*, 54(22): 6823. 2009.

[97] **Boyd, D.**, Knee-Joint Visualization. *The Journal of Bone & Joint Surgery*, 16(3): 671–680. 1934.

[98] **Lindblom, K.**, The arthrographic appearance of the ligaments of the knee joint. *Acta Radiologica*, 19(6): 582–600. 1938.

[99] **Reiser, M., Karpf, P., and Bernett, P.**, Diagnosis of chondromalacia patellae using CT arthrography. *European Journal of Radiology*, 2(3): 181–186. 1982.

[100] **De Filippo, M., Bertellini, A., Pogliacomi, F., Sverzellati, N., Corradi, D., Garlaschi, G., and Zompatori, M.**, Multidetector computed tomography arthrography of the knee: diagnostic accuracy and indications. *European Journal of Radiology*, 70(2): 342–351. 2009.

[101] **Berg, V.B., Lecouvet, F., Poilvache, P., Maldague, B., and Malghem, J.**, Spiral CT arthrography of the knee: technique and value in the assessment of internal derangement of the knee. *European Radiology*, 12(7): 1800–1810. 2002.

[102] **Bansal, P., Joshi, N., Entezari, V., Grinstaff, M., and Snyder, B.**, Contrast enhanced computed tomography can predict the glycosaminoglycan content and biomechanical properties of articular cartilage. *Osteoarthritis and Cartilage*, 18(2): 184–191. 2010.

[103] **Cockman, M., Blanton, C., Chmielewski, P., Dong, L., Dufresne, T., Hookfin, E., Karb, M., Liu, S., and Wehmeyer, K.**, Quantitative imaging of proteoglycan in cartilage using a gadolinium probe and microCT. *Osteoarthritis and Cartilage*, 14(3): 210–214. 2006.

[104] **Palmer, A.W., Guldberg, R.E., and Levenston, M.E.**, Analysis of cartilage matrix fixed charge density and three-dimensional morphology via contrast-enhanced microcomputed tomography. *Proceedings of the National Academy of Sciences*, 103(51): 19255–19260. 2006.

[105] **Minns, R. and Steven, F.**, The collagen fibril organization in human articular cartilage. *Journal of Anatomy*, 123(Pt 2): 437. 1977.

[106] **Nieminen, M.T., Rieppo, J., Silvennoinen, J., Töyräs, J., Hakumäki, J.M., Hyttinen, M.M., Helminen, H.J., and Jurvelin, J.S.**, Spatial assessment of articular cartilage proteoglycans with Gd-DTPA-enhanced T1 imaging. *Magnetic Resonance in Medicine*, 48(4): 640–648. 2002.

[107] **Rieppo, J., Töyräs, J., Nieminen, M.T., Kovanen, V., Hyttinen, M.M., Korhonen, R.K., Jurvelin, J.S., and Helminen, H.J.**, Structure-function relationships in enzymatically modified articular cartilage. *Cells Tissues Organs*, 175(3): 121–132. 2003.

[108] **Moody, H.R., Brown, C.P., Bowden, J., Crawford, R.W., McElwain, D., and Oloyede, A.**, In vitro degradation of articular cartilage: does trypsin treatment produce consistent results? *Journal of Anatomy*, 209(2): 259–267. 2006.

[109] **Buckwalter, J. and Mankin, H.**, Articular cartilage repair and transplantation. *Arthritis & Rheumatism*, 41(8): 1331–1342. 1998.

[110] **Harris, E.D., Parker, H.G., Radin, E.L., and Krane, S.M.**, Effects of proteolytic enzymes on structural and mechanical properties of cartilage. *Arthritis & Rheumatism*, 15(5): 497–503. 1972.

[111] **Linn, F.C. and Sokoloff, L.**, Movement and composition of interstitial fluid of cartilage. *Arthritis & Rheumatism*, 8(4): 481–494. 1965.

[112] Zeta Potential An Introduction in 30 Minutes. `https://www3.nd.edu/~rroeder/ame60647/slides/zeta.pdf`, accessed: 2016-03-21.